Electrochimica Acta 458 (2023) 142495

Contents lists available at ScienceDirect

Electrochimica Acta

journal homepage: www.journals.elsevier.com/electrochimica-acta

Improved photoelectrochemical hydrogen production performance of reduced graphene oxide-cadmium zinc sulfoselenide photoelectrodes prepared by a Facile In-situ Electrosynthesis method

Özlem UĞUZ NELİ, Özlem BUDAK, Atıf KOCA *

Department of Chemical Engineering, Engineering Faculty, Marmara University, 34854, Istanbul, Turkey

ARTICLE INFO

Keywords:
Electrodeposition
Cyclic voltammetry
Cadmium zinc sulfide
Cadmium zinc selenide
Reduced graphene oxide

ABSTRACT

Cadmium zinc sulfoselenide, CdZnSSe, and reduced graphene oxide-cadmium zinc sulfoselenide (RGO)-CdZnSSe composite-based photoelectrodes are fabricated using a facile, simultaneous co-electrodeposition by repetitive cyclic voltammetric (rCV) for the first time in literature. With this method, CdZnSSe particles are homogeneously decorated among the RGO sheets by controlling the composition of the composite structure and the film thickness with rCV. Photoelectrochemical, optical, and structural properties of photoelectrodes are evaluated to investigate their usability in photoelectrochemical hydrogen evolution. Decorating $Cd_{0.8}Zn_{0.2}S_{0.2}Se_{0.8}$ among RGO sheets leads to a slight red-shift of the absorption edge because of the less transparency of fabricated photoelectrode which decreases the band gap of composites. Among all $Cd_{0.8}Zn_{0.2}S_xSe_{1-x}$ ($x = 0.0, 0.2, 0.5, 0.8, 1.0$) photoelectrodes, $Cd_{0.8}Zn_{0.2}S_{0.2}Se_{0.8}$ demonstrates the sharp rise in photocurrent density (4.08 mA cm^{-2}). Decorating $Cd_{0.8}Zn_{0.2}S_{0.2}Se_{0.8}$ with RGO at an optimum composition jumps the photocurrent density up to 5.00 mA cm^{-2} in addition to the improved stability. The long-term stability of RGO(0.25)-$Cd_{0.8}Zn_{0.2}S_{0.2}Se_{0.8}$ is reported as 89.8% at the end of the 48th hour. The applied bias photon to current efficiency (ABPE) and Faradaic efficiency are obtained as 3.07% and 89.9%. Enhanced photoelectrochemical performance indicates the superiority of the proposed rCV technique for the fabrication of well-controlled photoelectrodes consisting of RGO—CdZnSSe composites.

1. Introduction

The rapid development of countries has led to increased levels of energy consumption over the last decades. However, the dependence of the major part of energy generation on fossil fuels has caused serious environmental pollution problems. Thus, the utilization of clean and sustainable energy that will be an alternative to fossil fuels has attracted global interest. Therefore, solar energy has been opted as a reasonable alternative energy source to eliminate the consumption of fossil fuel consumption [1–5]. One of the most popular energy generation methods based on the solar light harvest is photoelectrochemical hydrogen production and a considerable number of studies have been conducted mostly focusing on the development of various semiconductors including oxides, sulfides, selenides, and tellurides by modifying their structure and altering their band gaps. Among them, CdZnSSe semiconductors are fascinating due to their controllable compositions and particular sizes [6,7]. They exhibit the characteristic features of CdS, CdSe, ZnS, and ZnSe which have high absorption coefficients, a wide range of band gap energy, high sensitivity, good chemical stability, and electrical properties [8].

Recently, reduced graphene oxide (RGO) has been regarded as a vital supporting material for the fabrication of numerous effective photoanodes because of its unique properties, such as high charge-carrier mobility, stability, high conductivity, and large surface area [9]. In this way, combining RGO with CdZnSSe ensures ease the electron transfer, advances the photocurrent response, and prevents photo-corrosion of CdZnSSe, providing high PEC performance [10]. The study reported by Li et al. emphasized the vital role of RGO nanosheets on $Co_3O_4/Co(OH)_2$/RGO photocatalysts and their results indicate that RGO enhances the photocurrent by decreasing the nanoparticle aggregation and increasing the charge transfer rate [11].

CdZnSSe to be used as a photoelectrode material has been fabricated by several semiconductor preparation techniques such as thermal evaporation, chemical bath deposition, electrodeposition, spray

---

* Corresponding author.
E-mail address: akoca@marmara.edu.tr (A. KOCA).

https://doi.org/10.1016/j.electacta.2023.142495
Received 9 January 2023; Received in revised form 28 March 2023; Accepted 29 April 2023
Available online 30 April 2023

pyrolysis, hydrothermal, etc. [12]. Among all techniques, electrodeposition is the most remarkable one because of its advantages related to economy, operation facility on the large-area substrate, process continuity, and easy controllability of morphology. Furthermore, the electrodeposition method is a solution-based method that can be easily operated at low temperatures and has a high growth rate [13,14].

In the recent past, the number of studies of CdZnSSe composites and photoelectrodes in the photoelectrochemical field has increased, yet there is no reported work regarding the contribution of RGO in CdZnSSe thin films fabricated by one-step electrodeposition strategy. For example, Ibrahim et al. have published a study of RGO—$Cd_{0.5}Zn_{0.5}S$ which has been synthesized by the solvothermal method and they have shown that the photocurrent density is 185 μA when the light is on, and 122 μA when the light is off [15]. Zhuang et al. have reported a study designating to the photoelectrochemical performance of $CdSe@TiO_2$ core-shell nanorod arrays obtained by electrochemical deposition and their report exhibits a photocurrent density of 2.1 mA cm^{-2} under visible light irradiation [16]. In addition, Ayal et al. have developed CdSe supported titanium dioxide nanotube array as a semiconductor electrode for photoelectrochemical applications by using the electrodeposition technique. This study reveals that incorporating CdSe into titanium dioxide nanotube arrays provides a notable enhancement in the photoelectrochemical properties. They have reported the maximum photocurrent density of 1.94 mA cm^{-2} [17]. Izi et al. have fabricated ZnS thin films on a Mo substrate by electrodeposition and spray pyrolysis methods and have concluded that electrodeposited ZnS has a relatively lower band gap [18]. Kumarage et al. have studied the effect of the deposition method on the photoelectrochemical performance of CdS thin films. They have disclosed that electrodeposited CdS thin films exhibit better photoelectrochemical characteristics than chemical bath-deposited CdS thin films due to their improved interparticle connections and homogeneity [19]. Riveros et al. have electrodeposited composition-graded stacked $CdS_xSe_{(1-x)}$ thin films, but they haven't performed any application of the films. They deposited CdS and then exchanged S with Se in the structure with the gradual addition of SeO_2 in the electrodeposition bath. However, this method consisted of successive electrodeposition steps [20]. Besides, there are some studies that reported the photoelectrochemical performance of electrodeposited sulfide and selenide-based photoelectrodes conjugated with different transition metals. For instance, Cao et al. used template free electrodeposition method to fabricate SnS (nanorods)/Pt on fluorine-doped tin oxide (FTO) substrate and obtained the photocurrent density of 0.11 mA cm^{-2}. In their further experiments, they built SnS (nanorods)/CdS/Pt photoelectrodes with an enhanced photocurrent density of 0.45 mA cm^{-2} [21]. In another study presented by Matoba et al., $CuInS_2$ photoelectrode has been prepared by electrodeposition technique as a p-type $CuInS_2$ electrode and they have reported that Pt-In_2S_3/$CuInS_2$ electrode indicated effective PEC performance due to band-bending of the p-n junction between $CuInS_2$ and In_2S_3 [22]. Metal chalcogenide-based photoelectrodes have been frequently prepared by using visible-light responsible n-type semiconductors such as C_3N_4, WO_3, $BiVO_4$, and CdZnS [23,24]. In recent years, HER studies have also focused on the preparation of cathodic photoelectrodes for the water-splitting processes [25–27]. In our previous studies, we have reported the photoelectrochemical performance of hydrothermally prepared n-type RGO—CdS semiconductors [28] and electrodeposited RGO—CdZnS [29] structures. The maximum photocurrent is observed with the hydrothermally prepared ITO/RGO—CdS photoelectrode as 2.0 and 6.5 mA cm^{-2} at 0.0 and 0.54 V bias potentials, respectively [28]. In our other study, 1.38 mA cm^{-2} photocurrent density at 0.0 V bias potential is reported for the electrodeposited RGO(0.25)-$Cd_{0.8}Zn_{0.2}S$ structure [29]. As a continuity of our studies, here we have proposed to enhance the photoelectrochemical performances of transition metal chalcogenide-based photocatalysts by modifying them with new synthesis methods. Consequently, we have first of all synthesized well-controllable and reproducible CdZnSSe and RGO—CdZnSSe thin films on ITO substrates by using the facile one-step electrodeposition method (rCV) and the modified electrodes have been tested as photoanodes for the photoelectrochemical water splitting process. As far as we know, this study is the first example in the literature for the preparation of bimetallic sulfoselenide particles and their RGO composite structures with the rCV method. With this new method, it has been aimed to immobilize CdZnSSe particles among RGO sheets with the help of the rCV method. Moreover, we propose to evaluate the synergistic effect of RGO in CdZnSSe film on the photoelectrochemical performance for HER concerning increasing immobilization strength of the composite on the ITO surface, the conductivity of the films, and active sites of the composite structure which enable to enhance the photoelectrochemical performance.

2. Experimental

2.1. Materials

The materials and chemicals which are used in this study are listed in SM (Supplementary Material).

2.2. Preparation of $Cd_{0.8}Zn_{0.2}S_xSe_{1-x}$ and RGO—$Cd_{0.8}Zn_{0.2}S_xSe_{1-x}$ composite thin films

Electrodeposition with the repetitive cyclic voltammetry (rCV) method is used for the synthesis of $Cd_{0.8}Zn_{0.2}S_xSe_{1-x}$ ($x = 0.0$, 0.2, 0.5, 0.8, 1.0) thin films. The aqueous electrolytic bath for electrodeposition reactions consists of $Cd(CH_3COO)_2{\cdot}2H_2O$, $Zn(CH_3COO)_2{\cdot}2H_2O$, $Na_2S_2O_3$, Na_2SeSO_3, and EDTA. The concentrations of Cd, Zn, S, and Se precursors are determined based on the compositions of $CdZnS_xSe_{1-x}$ photoelectrodes (0.016 mol dm^{-3} $Cd(CH_3COO)_2{\cdot}2H_2O$, 0.004 mol dm^{-3} $Zn(CH_3COO)_2{\cdot}2H_2O$, $Na_2S_2O_3$, Na_2SeSO_3 ranging from 0.0 dm^{-3} to 0.040 mol dm^{-3}). The pH of the electrolytic bath is tuned at 8.7. Here, Na_2SeSO_3 solution is prepared at 80 °C for 4 h after dispersing Na_2SO_3 and Se powder in ultrapure water. Rinsed and cleaned ITO-coated glass slices serve as the substrates of the working electrode. The electrodeposition technique is conducted in a standard three-electrode system. The repetitive cyclic voltammetry technique is conducted at the rate of 100 mV s^{-1} between −1.5–1.0 V vs. Ag/AgCl. After that, ITO/$Cd_{0.8}Zn_{0.2}S_xSe_{1-x}$ photoelectrodes are thermally treated in a horizontal tube furnace at 350°C in the Argon atmosphere for 1 hour. The $Cd_{0.8}Zn_{0.2}S_{0.2}Se_{0.8}$ is determined as the best photoelectrode with the highest performance. The synthesis method of GO is given in the SM (Supplementary Material) [30]. RGO—$Cd_{0.8}Zn_{0.2}S_{0.2}Se_{0.8}$ photoelectrodes are prepared according to the procedure of $Cd_{0.8}Zn_{0.2}S_xSe_{1-x}$ mentioned above. Besides, the electrolyte also includes different amounts of GO powder such as 0.10 mg/ml, 0.25 mg/ml, and 0.50 mg/ml to be able to increase and evaluate the photoelectrochemical performance. GO powder is synthesized in our previous work [1]. After the reduction of GO, and redox reactions of the precursor ions during cyclic voltammetric electrodeposition, fabricated thin films are named as RGO(0.10)-$Cd_{0.8}Zn_{0.2}S_{0.2}Se_{0.8}$, RGO(0.25)-$Cd_{0.8}Zn_{0.2}S_{0.2}Se_{0.8}$, and RGO(0.50)- $Cd_{0.8}Zn_{0.2}S_{0.2}Se_{0.8}$.

2.3. Structural characterization techniques

The morphology and elemental identification of thin films are provided by using Field Emission Scanning Electron Microscopy (FESEM) equipped with an EDAX detector, FEI, Nonananosem 430, at the magnitudes of 5000 and 50,000. Raman spectroscopy is conducted with a Raman spectrometer (STEX-100) with a 514 nm excitation wavelength. X-ray photoelectron spectroscopy (XPS) analyses are carried out using a Thermo Scientific K-Alpha X-ray photoelectron spectrometer. The structural analyses are performed by using Rigaku Ultima IV, Cu Kalpha, 40 kV 30 mA at an angular range of 10 $° < 2\theta < 80°$. The thin films are examined by UV–vis diffuse reflectance spectrometer (PG instruments

T92+ UV/VIS) to determine their band gap energy.

2.4. Photoelectrochemical measurements

Photoelectrochemical properties of photoanodes are determined in a three-electrode cell set-up (Reference 1000B Potentiostat/Galvanostat/ ZRA). Here, Pt wire, Ag/AgCl, and photoanode electrodes are used as the counter electrode, the reference electrode, and the working electrode, respectively. The electrolyte is prepared as a mixture composed of 0.35 mol dm^{-3} Na_2S and 0.25 mol dm^{-3} Na_2SO_3 (pH=13.0). The power intensity of the HAL-320 Compact Xenon Light Source Solar Simulator is adjusted to 1.0×10^3 W m^{-2} (AM 1.5 G filter). The surface of the photoanode is exposed to solar light and the photoactive area of each photoanode is calculated as 0.8 cm^2 because of the electrodeposited ITO size of 0.8 cm x 1.0 cm. Linear sweep voltammograms (LSV) with a scan rate of 5 mV s^{-1} and chronoamperometry (CA) curves are obtained with light on-off irradiation tests, which are presented in SM as the experimental set-up (Fig. S1). Electrochemical impedance spectroscopy (EIS) is recorded in the dark with a frequency range of 10^5 to 10^{-2} Hz at a bias DC potential of 0 V. Mott-Shottky (M-S) measurements are examined with an AC frequency of 1 kHz with an amplitude of 5 mV. Evolved H_2 gas was collected in a Tedlar bag and analyzed with an online connected gas chromatography.

3. Results and discussion

Fig. S3 shows the CV curves of $Cd_{0.8}Zn_{0.2}S$ (Fig. S3a), $Cd_{0.8}Zn_{0.2}Se$ (Fig. S3b), and $Cd_{0.8}Zn_{0.2}S_{0.2}Se_{0.8}$ (Fig. S3c). The reduction and oxidation peaks for the formation of these thin films are explained in detail in Supplementary Material (SM). Fig. 1 represents the CV profile of RGO (0.25)-$Cd_{0.8}Zn_{0.2}S_{0.2}Se_{0.8}$ thin film formation on ITO substrate between −1.5–1.0 V vs Ag/AgCl. When compared with Fig. S3c, it is clear that a new wave is observed at 0.50 V due to the oxidation of reduced film of RGO on the electrode surface and the general trend of the CVs in Fig. 1 clearly shows the coating of RGO on ITO surface and incorporation of $Cd_{0.8}Zn_{0.2}S_{0.2}Se_{0.8}$ structure between RGO sheets. The proposed voltammetric mechanisms and structures of the modified electrodes are supported with various morphological and optical characterizations discussed below. Especially, the Raman spectra of the films discussed below support the presence of RGO sheets on the electrode surface.

Fig. 2 demonstrates the Raman spectra of $Cd_{0.8}Zn_{0.2}S_{0.2}Se_{0.8}$ (a) and RGO(0.25)-$Cd_{0.8}Zn_{0.2}S_{0.2}Se_{0.8}$ (b) recorded with laser excitation at 532 nm. The bands positioned at 177 cm^{-1}, 202 cm^{-1} 418 cm^{-1}, and 615 cm^{-1} belong to the Raman modes of TO (transverse optical phonon), 1LO (longitudinal optical phonon), and 2LO bands of CdZnSSe (Fig. 2a) [31]. D and G bands of synthesized GO are given in Fig. S4. D and G bands exhibit peaks at 1359 cm^{-1} and 1596 cm^{-1}. These peaks of GO are fitted to Gaussian functions (R^2=0.992) and the intensity ratio (I_D/I_G) for GO is calculated as 0.67. The D and G bands positioned at 1359 cm^{-1} and 1562 cm^{-1} belong to RGO of RGO(0.25)-$Cd_{0.8}Zn_{0.2}S_{0.2}Se_{0.8}$ photoelectrode and they give the best fit to Gaussian functions (R^2=0.989) (Fig. 2b). Upon reduction of GO during electrodeposition, I_D/I_G increases to 0.99 due to the restoration of sp^2 carbon atoms and decrease in mean sizes of sp^2 domains. Furthermore, the positions of the D and G bands shift and get closer to each other for RGO [32].

The FESEM images of $Cd_{0.8}Zn_{0.2}S_{0.2}Se_{0.8}$ and RGO(0.25)-$Cd_{0.8}Zn_{0.2}S_{0.2}Se_{0.8}$ thin films recorded at low (a and b) and high (c and d) magnifications are presented on Fig. 3. As shown in these figures, thin films have compact and dense surface morphology with some cluster formation on some points. However, with the presence of RGO in the structure, the cluster formation has been diminished and a smoother surface has been achieved (Fig. 3b). At high magnifications (Fig. 3c and Fig. 3d), RGO sheets are clearly observed around $Cd_{0.8}Zn_{0.2}S_{0.2}Se_{0.8}$ particles. EDS spectra demonstrate the existence of Cd, Zn, S, Se, C, and O in RGO(0.25)-$Cd_{0.8}Zn_{0.2}S_{0.2}Se_{0.8}$ thin film fabricated on ITO (Fig. S5). Furthermore, the detected In and Si peaks are attributed to the indium tin oxide structure of the ITO and the glass substrate. RGO in the composite thin film is verified with the presence of C and O elements.

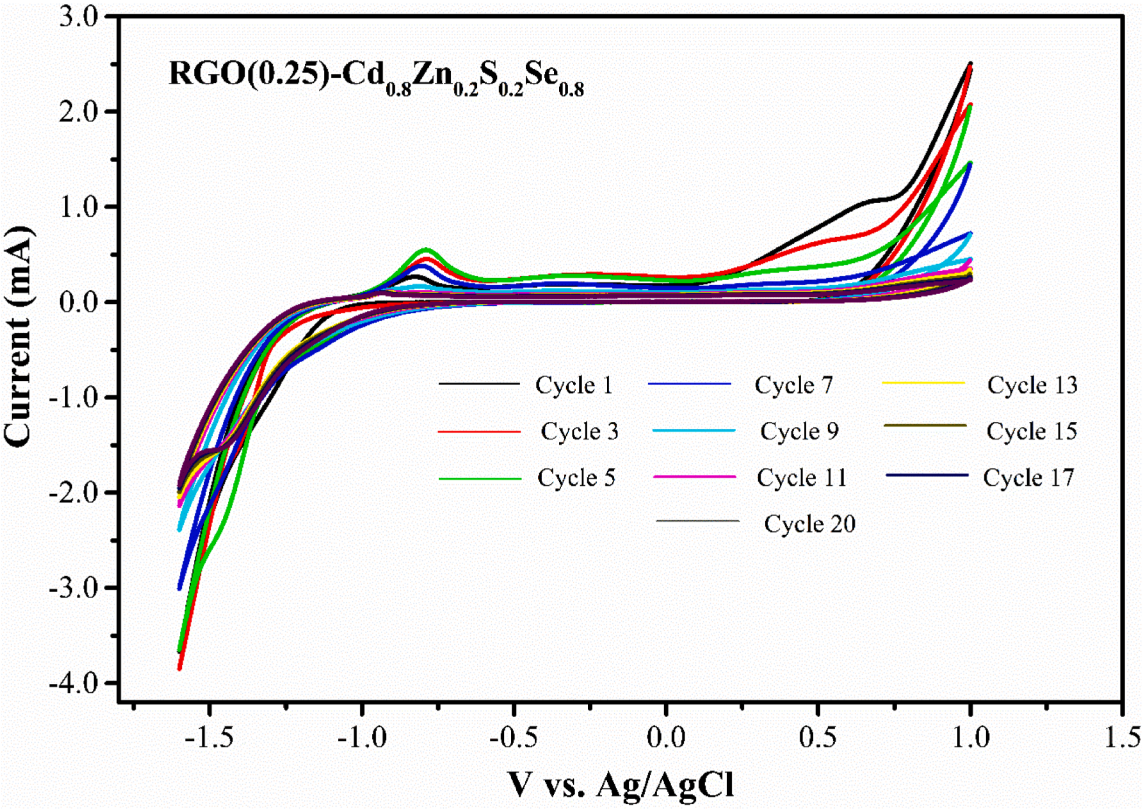

Fig. 1. rCV curves for the fabrication of RGO(0.25)-$Cd_{0.8}Zn_{0.2}S_{0.2}Se_{0.8}$.

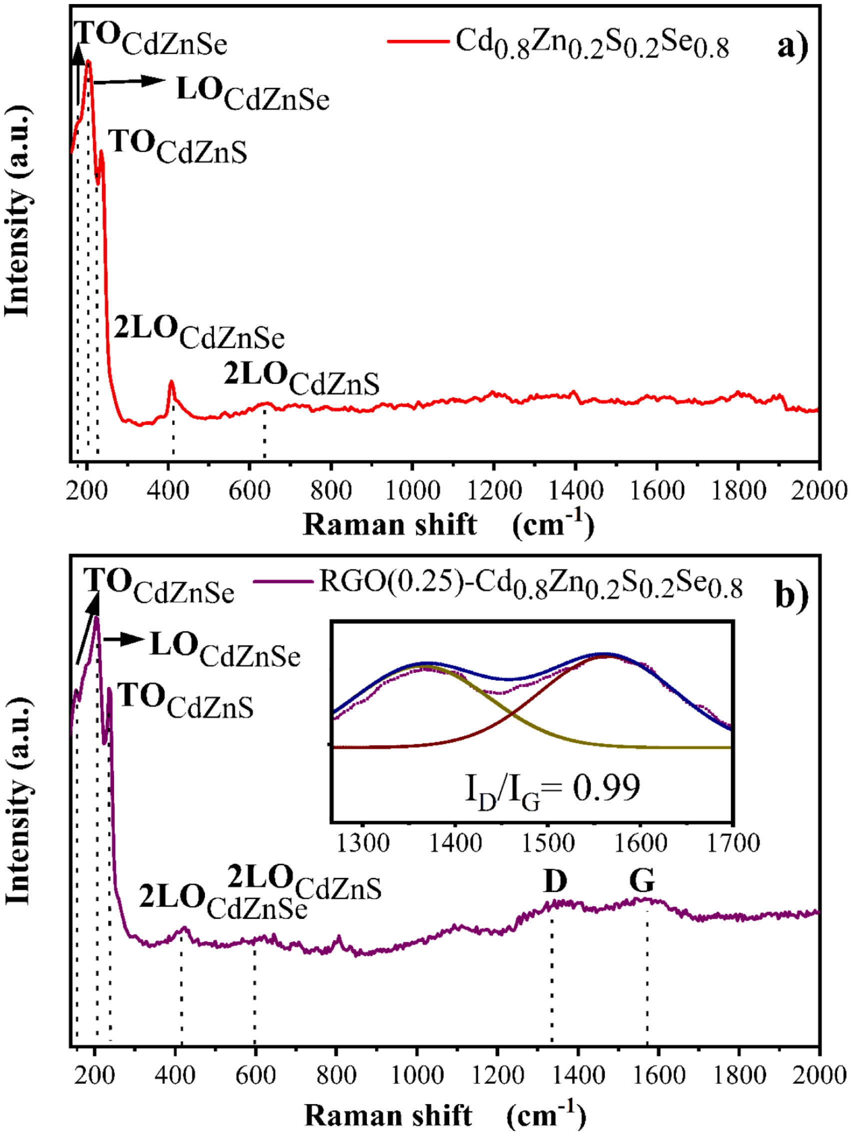

Fig. 2. Raman spectra of a) $Cd_{0.8}Zn_{0.2}S_{0.2}Se_{0.8}$, b) RGO(0.25)-$Cd_{0.8}Zn_{0.2}S_{0.2}Se_{0.8}$ thin films.

XPS measurements are carried out to investigate the chemical states and surface chemical compositions of composites. The XPS full spectrum (survey) of RGO(0.25)-$Cd_{0.8}Zn_{0.2}S_{0.2}Se_{0.8}$ confirms the presence of the characteristic peaks of Cd 3d, Zn 2p, S 2p, Se 3d, C 1 s and O 1 s (Fig. 4). XPS spectrum of each element is deconvoluted into peaks by Gaussian fitting through Origin software. The binding energies of Cd 3d are positioned at 405.5 eV ($3d_{5/2}$) and 412.2 eV ($3d_{3/2}$) and the difference in binding energy between two peaks is 6.7 eV, indicating that Cd is present in the form of Cd^{2+} [33]. The Zn 2p spectrum is fitted by deconvoluting the two $2p_{3/2}$ and $2p_{1/2}$ peaks at 1024 eV and 1047 eV, impaired with a satellite peak, respectively [34]. The spin–orbit splitting of Zn $2p_{3/2}$ and $2p_{1/2}$ is 23 eV which is attributed to ZnS and ZnSe bonding.

S 2p XPS spectrum displays two noticeable peaks located at 160.6 eV and 165.7 eV, which is related to the core levels of $2p_{3/2}$ and $2p_{1/2}$, respectively. Se 3d spectrum is deconvoluted into three peaks at 54.5 and 53.6 eV which are assigned to $3d_{3/2}$ and $3d_{5/2}$. The broad peak at 59 eV can arise from the Se-O bonding structure, which results from the oxidation state of the Se species [35]. Additionally, In 3d and O 1 s peaks on the overall XPS spectrum are attributed to the substrate material. Apart from the Cd 3d, Zn 2p, S 2p, and Se 3d spectra, the peaks of C 1 s and O 1 s spectra are also investigated. C 1 s spectrum is decomposed into three peaks composed of C—C/C = C (285.0 eV), C—O (286.8 eV), and C = O (289.2 eV), indicating the presence of RGO [36]. Oxygenated functional groups of RGO are observed in the form of C = O/O = C—OH (529.7 eV), C—O (531.7 eV), H_2O (533.7 eV), C—OH (536.0 eV) [37]. The XPS results are compatible with Raman spectrums given in Fig. 2. The atomic compositions and atomic ratios of the elements of RGO—$Cd_{0.8}Zn_{0.2}S_{0.2}Se_{0.8}$ are given in Table S1. According to the data, it is verified that the atomic ratio of the elements $Cd_xZn_{(1-x)}S_ySe_{(1-y)}$ of RGO—$Cd_{0.8}Zn_{0.2}S_{0.2}Se_{0.8}$ is found as $Cd_{0.81}Zn_{0.19}S_{0.22}Se_{0.78}$ ($Cd_xZn_{(1-x)}S_ySe_{(1-y)}$), and for the RGO, C:O ratio is determined as 0.68:0.32. In addition, the XPS spectrum of $Cd_{0.8}Zn_{0.2}S_{0.2}Se_{0.8}$ is represented in Fig. S6. The C1s element on the survey spectrum can be assigned to the trace hydrocarbon coming from the XPS instrument since it is used as the reference peak [38].

Fig. 5 shows the XRD patterns for $Cd_{0.8}Zn_{0.2}Se$, $Cd_{0.8}Zn_{0.2}S_{0.2}Se_{0.8}$, and RGO(0.25)-$Cd_{0.8}Zn_{0.2}S_{0.2}Se_{0.8}$ and they indicate peaks centered at around 2θ=24.1°, 25.4°, 27.3°, 42.1°, 49.9°. These peaks can be ascribed to the (100), (002), (101), (110), and (112) planes of the hexagonal structure of CdZnSSe (JCPDS Card no. 49–1459) [39]. The (002) and (102) planes of RGO are positioned at 2θ=26.40° and 45.18°, respectively. Thus, the pattern of RGO(0.25)-$Cd_{0.8}Zn_{0.2}S_{0.2}Se_{0.8}$ reveals that the intensity of peaks recorded between 20°- 27° are higher than

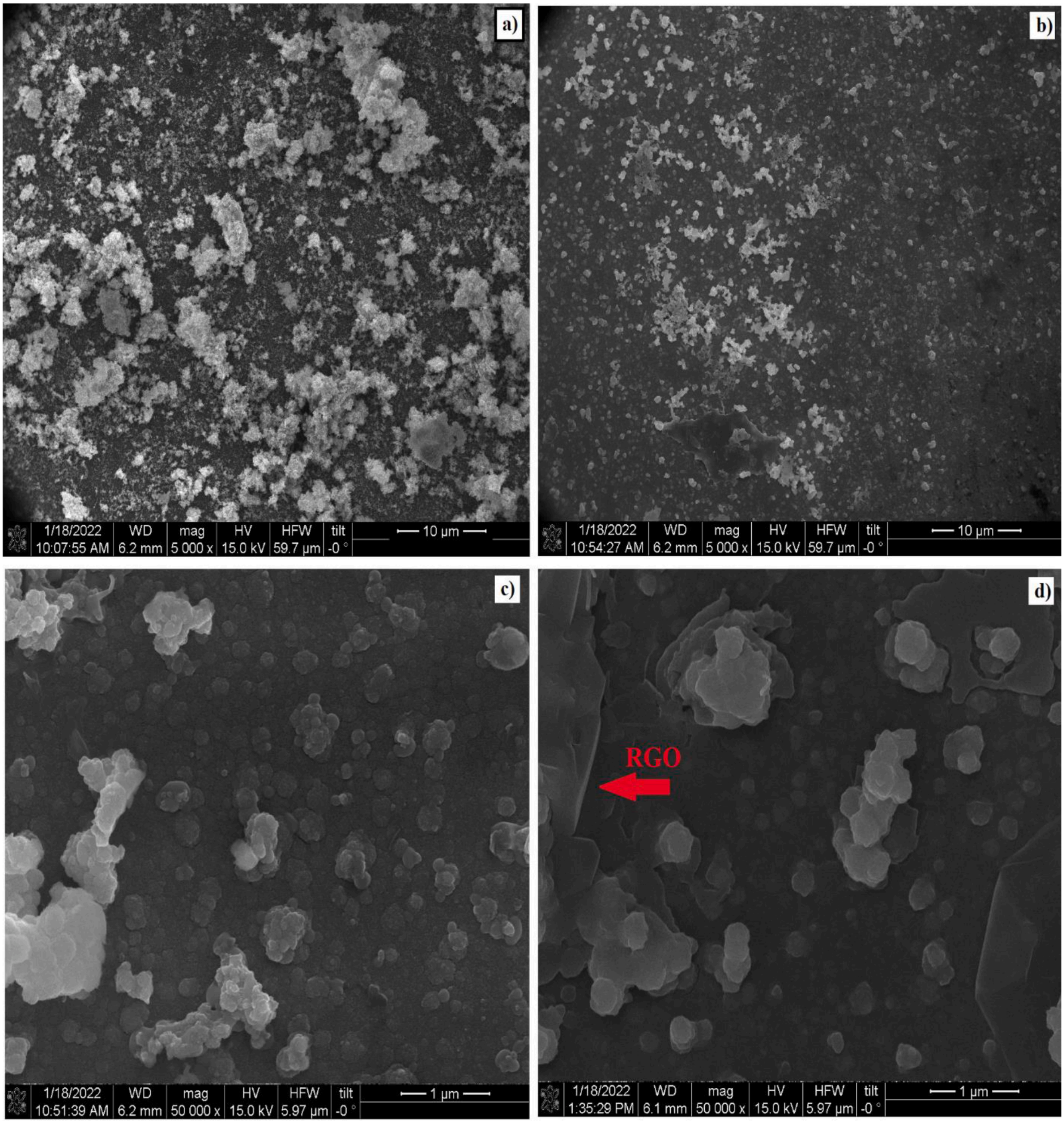

Fig. 3. FESEM images of thin films at low (x5000) magnification a) $Cd_{0.8}Zn_{0.2}S_{0.2}Se_{0.8}$ b) RGO(0.25)-$Cd_{0.8}Zn_{0.2}S_{0.2}Se_{0.8}$; FESEM images of thin films at high (x50000) magnification c) $Cd_{0.8}Zn_{0.2}S_{0.2}Se_{0.8}$, d) RGO(0.25)-$Cd_{0.8}Zn_{0.2}S_{0.2}Se_{0.8}$.

$Cd_{0.8}Zn_{0.2}Se$ and a small new peak at 45.18° is observed due to the presence of RGO in the structure. Debye-Scherrer's formula (given in SM) is employed to determine the average crystallite size [40]. The average crystallite sizes of $Cd_{0.8}Zn_{0.2}S_{0.2}Se_{0.8}$ and RGO (0.25)-$Cd_{0.8}Zn_{0.2}S_{0.2}Se_{0.8}$ are calculated as 99.5 and 80.0 nm, respectively. RGO contribution provides a smaller crystallite size, enhancing the photoelectrochemical performance [41].

To evaluate the optical properties of photoelectrodes, UV–vis DRS spectra are recorded. Fig. 6a and Fig. 6b give the reflectance-wavelength curves and Tauc plots of $Cd_{0.8}Zn_{0.2}S$, $Cd_{0.8}Zn_{0.2}Se$, $Cd_{0.8}Zn_{0.2}S_{0.2}Se_{0.8}$, and RGO(0.25)-$Cd_{0.8}Zn_{0.2}S_{0.2}Se_{0.8}$, respectively. Fig. 6a shows that introducing RGO to the $Cd_{0.8}Zn_{0.2}S_{0.2}Se_{0.8}$ photoelectrode leads to a slight red-shift of the absorption edge because of the less transparency of the fabricated photoelectrode [42]. The band gap values of RGO (0.25)-$Cd_{0.8}Zn_{0.2}S_{0.2}Se_{0.8}$ and $Cd_{0.8}Zn_{0.2}S_{0.2}Se_{0.8}$ are estimated based on the Kubelka-Munk function (given in SM) [43]. The band gap energies are determined as 1.75, 1.84, 1.80, and 2.47 eV for $Cd_{0.8}Zn_{0.2}Se$, $Cd_{0.8}Zn_{0.2}S_{0.2}Se_{0.8}$, RGO(0.25)-$Cd_{0.8}Zn_{0.2}S_{0.2}Se_{0.8}$, and $Cd_{0.8}Zn_{0.2}S$ photoelectrodes (Fig. 6b). RGO(0.25)-$Cd_{0.8}Zn_{0.2}S_{0.2}Se_{0.8}$ possesses lower band gap than $Cd_{0.8}Zn_{0.2}S_{0.2}Se_{0.8}$ due to the interaction of the RGO sheets with $Cd_{0.8}Zn_{0.2}S_{0.2}Se_{0.8}$ particles[44].

Photoelectrochemical performances of photoelectrodes are studied through a three-electrode system (Reference electrode: Ag/AgCl, Counter electrode: Pt wire, Working electrode: ITO coated glass substrate) in Na_2S/Na_2SO_3 sacrificial reagent. Here, sulfide (S^{2-}) and sulfite (SO_3^{2-}) anions act as efficient reducing agents to scavenge photogenerated holes to oxidize S^{2-} into disulfide (S_2^{2-}) anions, and SO_3^{2-} into sulfate (SO_4^{2-}) and thiosulfate $S_2O_3^{2-}$ [45]. Fig. 7 displays the linear sweep voltammograms (LSVs) of fabricated photoelectrodes under chopped 1 Sun (AM 1.5 G) illumination. Fig. 7a represents the LSV

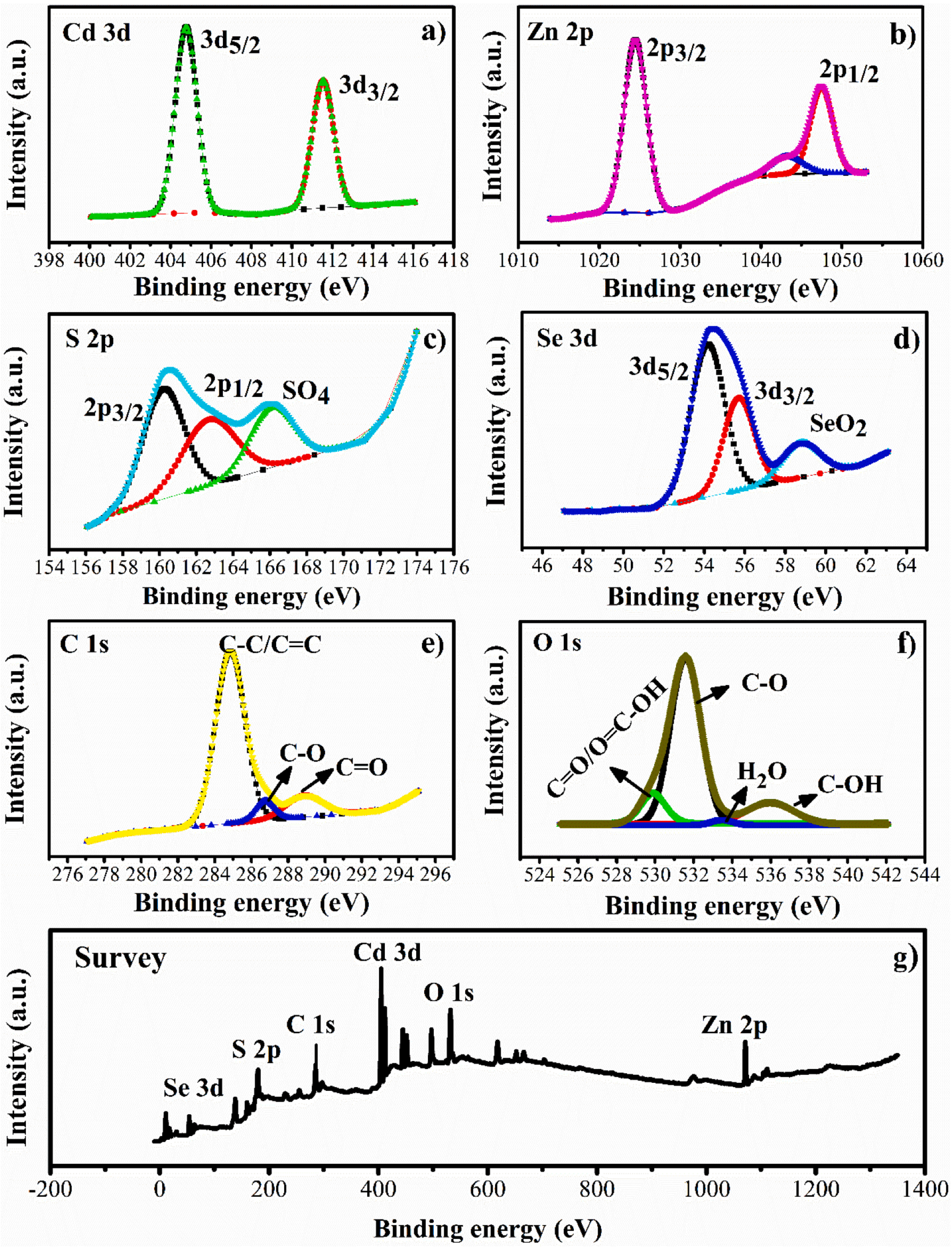

Fig. 4. X-ray photoelectron spectroscopy (XPS) spectra of RGO(0.25)-$Cd_{0.8}Zn_{0.2}S_{0.2}Se_{0.8}$ a) Cd 3d, b) Zn 2p, c) S 2p, d) Se 3d, e) C 1 s, f) O 1 s, g) Survey.

curves of $Cd_{0.8}Zn_{0.2}S$, $Cd_{0.8}Zn_{0.2}S_{0.8}Se_{0.2}$, $Cd_{0.8}Zn_{0.2}S_{0.5}Se_{0.5}$, $Cd_{0.8}Zn_{0.2}S_{0.2}Se_{0.8}$, $Cd_{0.8}Zn_{0.2}Se$ annealed at 350°C under Argon gas flow for 1 h. Annealing treatment is necessary to suppress electron-hole charge recombination by improving the contact between the thin film and ITO substrate [46]. Linear sweep voltammograms (LSVs) are obtained in a potential range between −0.2 V and 1.8 V vs. RHE under light on-light off cycles at 100 mV intervals. RHE stands for the reversible hydrogen electrode (RHE) scale converted by using the Nernst equation given in SM [47]. According to Fig. 7a, $Cd_{0.8}Zn_{0.2}S_{0.2}Se_{0.8}$ photoelectrode exhibits relatively higher photocurrent density among all tested photoelectrodes. This situation arises from the low rate of electron-hole recombination experienced during LSV analysis. Fig. 7b demonstrates linear sweep voltammograms of RGO (0.10)-$Cd_{0.8}Zn_{0.2}S_{0.2}Se_{0.8}$, RGO(0.25)-$Cd_{0.8}Zn_{0.2}S_{0.2}Se_{0.8}$, RGO (0.50)-$Cd_{0.8}Zn_{0.2}S_{0.2}Se_{0.8}$ photoelectrodes. The light is switched on and off at regular intervals, causing a fast current upshot followed by decay. The dark current is observed as the applied potential increases, which might occur due to the leakage of charge carriers near an electrode

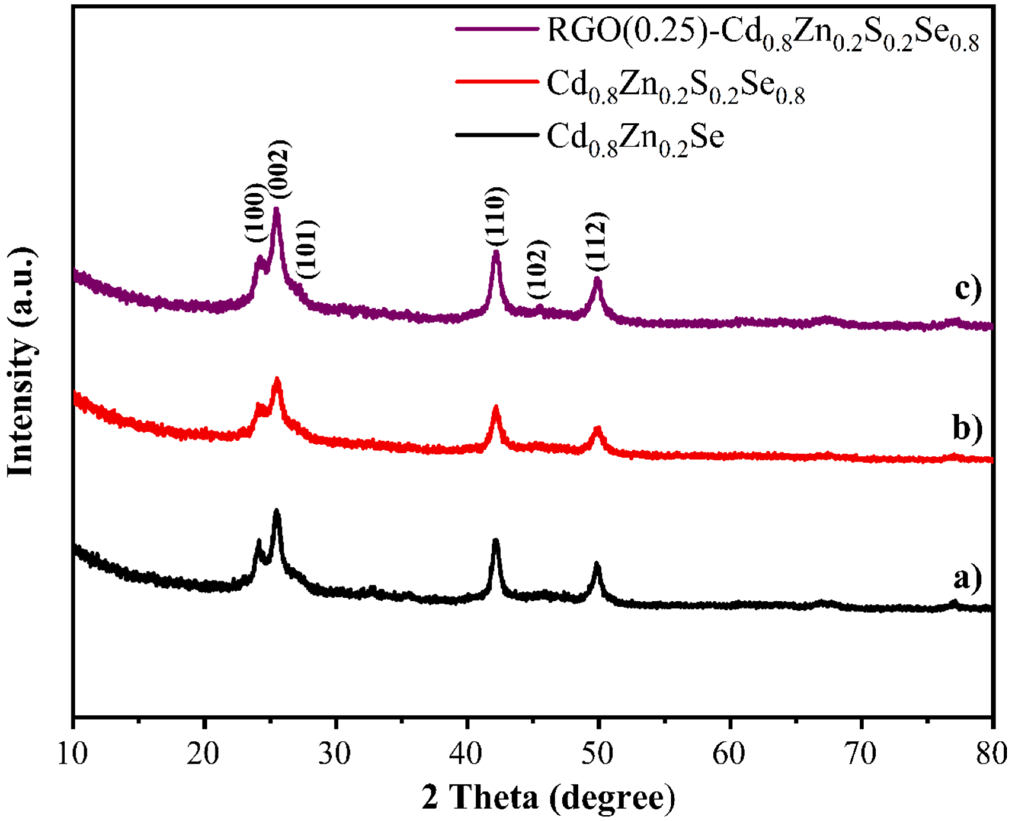

Fig. 5. XRD patterns of fabricated thin films a) $Cd_{0.8}Zn_{0.2}Se$, b) $Cd_{0.8}Zn_{0.2}S_{0.2}Se_{0.8}$ and c) RGO(0.25)-$Cd_{0.8}Zn_{0.2}S_{0.2}Se_{0.8}$.

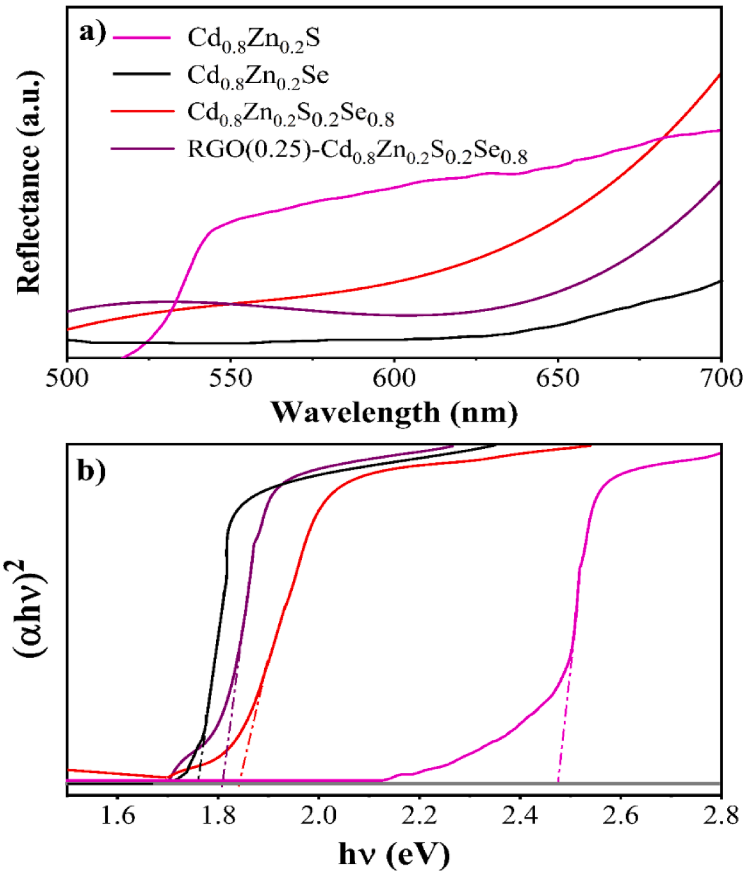

Fig. 6. a) UV–vis DRS and b) Tauc plots of $Cd_{0.8}Zn_{0.2}S$, $Cd_{0.8}Zn_{0.2}Se$, $Cd_{0.8}Zn_{0.2}S_{0.2}Se_{0.8}$ and RGO(0.25)-$Cd_{0.8}Zn_{0.2}S_{0.2}Se_{0.8}$ thin films.

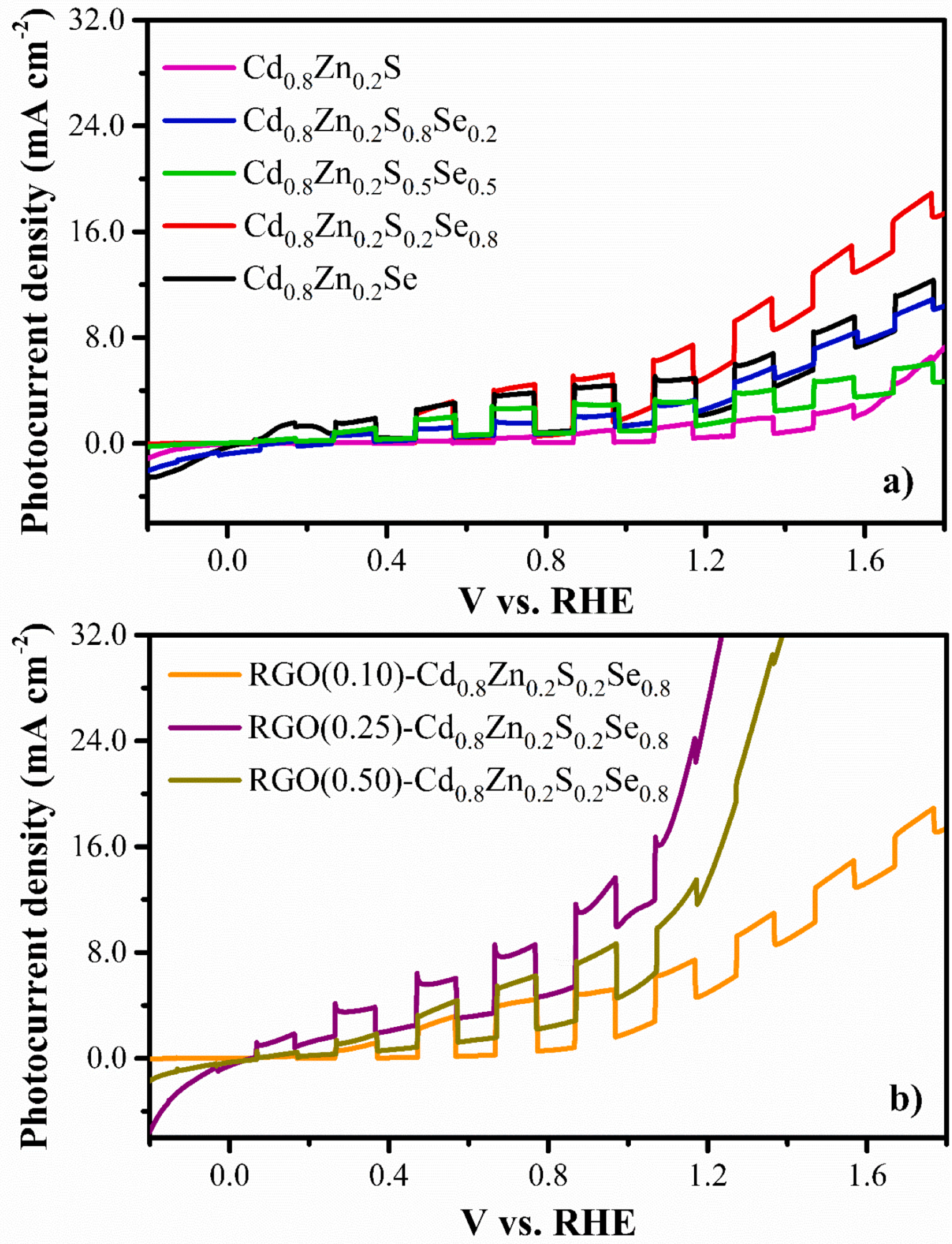

Fig. 7. LSV curves of a) $Cd_{0.8}Zn_{0.2}S_xSe_{1-x}$ (x = 0.0, 0.2, 0.5, 0.8, 1.0) and b) RGO(0.10, 0.25, 0.50)-$Cd_{0.8}Zn_{0.2}S_{0.2}Se_{0.8}$ photoelectrodes.

surface into the electrolyte [48]. RGO acts as a conductive-bridge linker, promotes electron-hole separation, and improves photocurrent to different degrees [49]. Several reports in the literature are in accordance with this statement [50–53]. Nevertheless, excessive mass loading of RGO in the photoelectrode may result in blocking the active species and prevention of the light absorption [54]. As a consequence, an optimization of the RGO amount is required to utilize solar energy effectively and improve the photoelectrochemical performance [55]. Fig. 7b clearly suggests that RGO(0.25)- $Cd_{0.8}Zn_{0.2}S_{0.2}Se_{0.8}$ provides superior photoelectrochemical characteristics.

The photoelectrochemical performances of photoelectrodes are evaluated in the three-electrode system via chronoamperometry technique at room temperature. The transient photocurrent density (I)-time (t) curves of $Cd_{0.8}Zn_{0.2}S$, $Cd_{0.8}Zn_{0.2}S_{0.8}Se_{0.2}$, $Cd_{0.8}Zn_{0.2}S_{0.5}Se_{0.5}$, $Cd_{0.8}Zn_{0.2}S_{0.2}Se_{0.8}$, $Cd_{0.8}Zn_{0.2}Se$ (Fig. 8a), and RGO(0.10)-$Cd_{0.8}Zn_{0.2}S_{0.2}Se_{0.8}$, RGO(0.25)-$Cd_{0.8}Zn_{0.2}S_{0.2}Se_{0.8}$, RGO(0.50)-$Cd_{0.8}Zn_{0.2}S_{0.2}Se_{0.8}$ (Fig. 8b) photoelectrodes are obtained for six light on-light off cycles at 50 s intervals. The photocurrent densities are calculated according to the difference between the observed photocurrent densities under light on-light off conditions. The I-t curves illustrated in Fig. 8a show that $Cd_{0.8}Zn_{0.2}S$, $Cd_{0.8}Zn_{0.2}S_{0.8}Se_{0.2}$, $Cd_{0.8}Zn_{0.2}S_{0.5}Se_{0.5}$, $Cd_{0.8}Zn_{0.2}S_{0.2}Se_{0.8}$, $Cd_{0.8}Zn_{0.2}Se$ exhibit the photocurrent densities of 0.94, 1.34, 2.34, 4.08, 3.07 mA cm^{-2} at 0.8 V bias (vs. RHE) under chopped solar light irradiation (150 W Xe light, light intensity: 100 mW cm^{-2}) It is observed that all $Cd_{0.8}Zn_{0.2}S_xSe_{1-x}$ (x = 0.0, 0.2, 0.5, 0.8, 1.0) photoelectrodes demonstrate a steep rise in photocurrent when the light is on, yet the photocurrent drops rapidly in dark condition. During repetitive on-off illumination cycles, all photoelectrodes reveal n-type conductivity characteristics. Fig. 8b indicates that RGO suppresses the recombination of photoinduced charges.

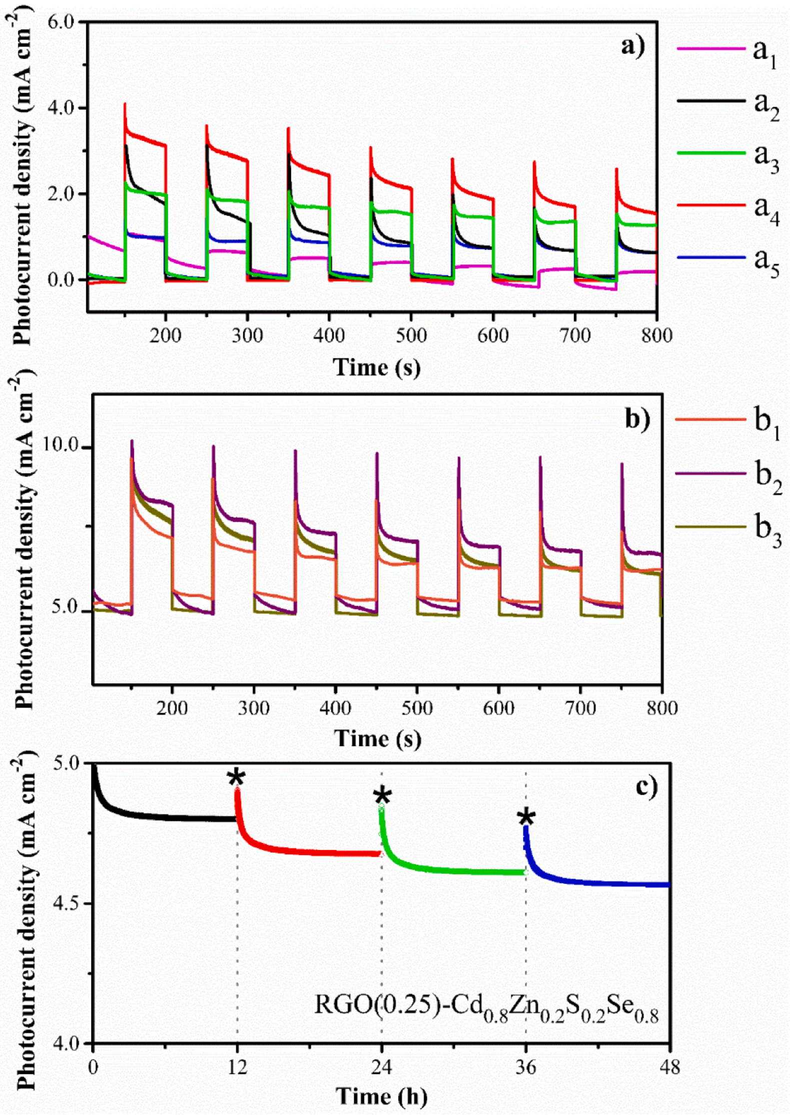

Fig. 8. Chronoamperometric photocurrent density-time curves of a) $Cd_{0.8}Zn_{0.2}$ S_xSe_{1-x} ($x = 0.0, 0.2, 0.5, 0.8, 1.0$). a_1: $Cd_{0.8}Zn_{0.2}S$, a_2: $Cd_{0.8}Zn_{0.2}Se$, a_3: $Cd_{0.8}Zn_{0.2}S_{0.5}Se_{0.5}$, a_4: $Cd_{0.8}Zn_{0.2}S_{0.2}Se_{0.8}$ a_5: $Cd_{0.8}Zn_{0.2}S_{0.8}Se_{0.2}$ and b) RGO(0.10, 0.25, 0.50)-$Cd_{0.8}Zn_{0.2}S_{0.2}Se_{0.8}$ photoelectrodes, b_1: RGO(0.10)-$Cd_{0.8}Zn_{0.2}S_{0.2}Se_{0.8}$, b_2: RGO(0.25)-$Cd_{0.8}Zn_{0.2}S_{0.2}Se_{0.8}$, b_3: RGO(0.50)-$Cd_{0.8}Zn_{0.2}S_{0.2}Se_{0.8}$ c) the long term stability measurement of RGO(0.25)-$Cd_{0.8}Zn_{0.2}S_{0.2}Se_{0.8}$ photoelectrode under the continuous simulated sunlight illumination (* represents the time sacrificial electrolyte is renewed).

Namely, the photocurrent density of $Cd_{0.8}Zn_{0.2}S_{0.2}Se_{0.8}$ jumps from 4.08 mA cm^{-2}, to 4.21, 5.00, and 4.51 mA cm^{-2} for RGO(0.10)-$Cd_{0.8}Zn_{0.2}S_{0.2}Se_{0.8}$, RGO(0.25)-$Cd_{0.8}Zn_{0.2}S_{0.2}Se_{0.8}$, RGO(0.50)-$Cd_{0.8}Zn_{0.2}S_{0.2}Se_{0.8}$ photoelectrodes, respectively. Fig. 8c reveals the long-term chronoamperometric stability measurement of RGO(0.25)-$Cd_{0.8}Zn_{0.2}S_{0.2}Se_{0.8}$ photoelectrode under the continuous simulated

Table 1
A representative summary of the performance of related photoelectrodes reported in the literature.

Photoelectrode/ Substrate	Preparation Method	Post-treatment temperature	Sacrificial reagent	Light intensity (mW cm^{-2})	Applied Potential	Photocurrent density (mA/cm^2)	Ref.
ZnO/ZnSe/CdSe /Zn foil	Hydrothermal/ion exchange	–	Na_2S/Na_2SO_3	100	−0.2 V vs. Ag/AgCl	3.008	[59]
TiO_2/MoS_2 /FTO	Hydrothermal	500 °C	Na_2SO_4	100	1.23 V vs. RHE	1.56	[60]
$CdSe_{0.6}S_{0.4}S$/ITO	Spin coating	–	Na_2SO_4	100	−0.6 V vs. SCE	0.68	[61]
CdSe/ZnSe/ZnO/FTO	Electrodeposition/ion exchange	–	Na_2S/Na_2SO_3	100	0 V vs. Ag/AgCl	3.2	[62]
Cu:$CdS_{0.7}Se_{0.3}$/Pt	PVD/DC sputtering	–	Na_2SO_4	100	−0.12 V vs. RHE	0.82	[63]
Fe_2O_3/MoS_2/FTO	Hydrothermal/drop casting	450 °C (Air)	NaOH	100	0.6 V vs. Ag/AgCl	1.56	[64]
$BiVO_4/Fe_2O_3/ZnFe_2O_4$	Spray pyrolysis	450 °C	NaOH	100	1.23 V vs. RHE	2.47	[65]
$TiO_2/SnS_2/CoO_x$/FTO	Hydrothermal/ solvothermal	550°C(air)	Na_2SO_4	100	1.23 V vs. RHE	1.05	[66]
TiO_2/CdS/MoS_2/FTO	CBD and SILAR	–	Na_2S/ Na_2SO_3	100	0.9 V vs. RHE	3.25	[67]
$Cd_{0.8}Zn_{0.2}S_{0.2}Se_{0.8}$/ITO	**One step electrodeposition**	**350°C (Ar)**	**Na_2S/Na_2SO_3**	**100**	**0.80 V vs. RHE**	**4.08**	**tw**
RGO(0.25)/ $Cd_{0.8}Zn_{0.2}S_{0.2}Se_{0.8}$/ITO	**One step electrodeposition**	**350°C (Ar)**	**Na_2S/Na_2SO_3**	**100**	**0.80 V vs. RHE**	**5.00**	**tw**

sunlight illumination at 0.8 V vs. RHE. Decreasing the photocurrent density with time is attributed to the decrease of the concentration of the sacrificial reagent in addition to the slight decrease of the electrode stability. Thus, at the end of each 12th hour, the sacrificial reagent in the three-electrode system is renewed. The photoelectrode maintains 89.8% of its initial photocurrent density at the end of 48th hour, which is comparable to the reported stability results of the photoelectrodes [56–58]. Operation of the PEC reaction in a flow cell may prevent the influence of the sacrificial reagent concentration change on the photocurrent density in practical applications.

Table 1 gives a summary of the photocurrent densities of some related photoelectrodes stated in the literature. There are some methods to fabricate metal sulfides, selenides and oxides and RGO based photoelectrodes such as electrodeposition, spray pyrolysis, spin coating, drop coating, hydrothermal, solvothermal, chemical bath deposition, successive ionic layer adsorption, and reaction. In given studies, annealing is performed within the range of 250–550°C under air and argon atmosphere. In Table 1, the photocurrent densities obtained with various metal chalcogenides are generally reported between 0.68–3.25 mA cm^{-2}. In the literature, there is no report which is based on facile, one-step electrodeposition of RGO—CdZnSSe on any substrate. Moreover, the PEC performance obtained in this study is among the highest ones.

The hydrogen production rate of RGO(0.25)-$Cd_{0.8}Zn_{0.2}S_{0.2}Se_{0.8}$ photoelectrode is determined with the Faraday's equation (given in SM) and the hydrogen production rate of RGO(0.25)-$Cd_{0.8}Zn_{0.2}S_{0.2}Se_{0.8}$

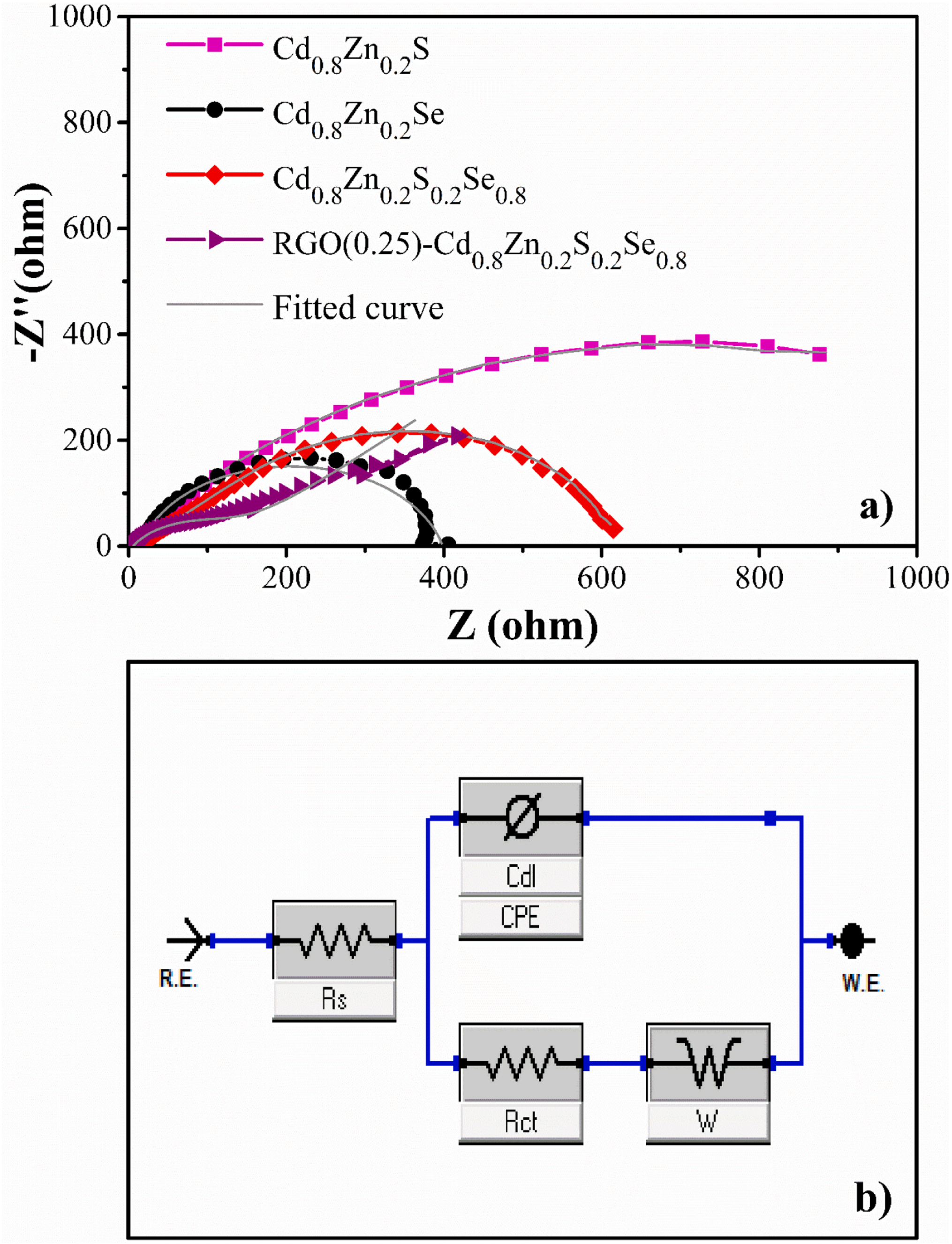

Fig. 9. Nyquist plots of a) $Cd_{0.8}Zn_{0.2}S_xSe_{1-x}$ ($x = 0.0, 0.2, 0.5, 0.8, 1.0$) and RGO(0.10, 0.25, 0.50)-$Cd_{0.8}Zn_{0.2}S_{0.2}Se_{0.8}$ photoelectrodes, b) Equivalent circuit model used for EIS data fitting (R.E.: Reference electrode, W.E: Working electrode, R_s: Series resistance, R_{ct}: Charge transfer resistance, CPE: Constant phase element, W: Finite-length Warburg element).

photoelectrode is calculated as 94.9 μmole h^{-1}. Moreover, this amount is supported by GC analysis connected online to the reactor.

The charge transfer at the semiconductor-electrolyte interface has been examined with EIS analysis. EIS measurements are performed in the frequency range of 10^5 to 10^{-2} Hz under dark conditions. Fig. 9a displays Nyquist plots of the photoelectrodes. The semicircular radius and inclined line are associated with the mechanism of charge transfer and photoelectrode kinetics. The smaller the semicircular radius is, the lower the charge transfer resistance [68]. Experimental results are fitted by using an equivalent Randles circuit model with a Warburg element as given in Fig. 9b. R_s corresponds to series resistance which combines ITO, sacrificial electrolyte, and external contact for the electrochemical device. R_{ct} accounts for the charge transfer resistance at the semiconductor-electrolyte interface [69]. The constant phase element (CPE) defines the capacitance, resulting from the formation of a double layer in the photoelectrode. The adopted EIS fitting model yields R_s and R_{ct} values for RGO(0.25)-$Cd_{0.8}Zn_{0.2}S_{0.2}Se_{0.8}$, $Cd_{0.8}Zn_{0.2}S_{0.2}Se_{0.8}$, $Cd_{0.8}Zn_{0.2}Se$ and $Cd_{0.8}Zn_{0.2}S$ as 7.3 and 145.1 Ω cm^{-2}, 13.6 and 715.5 Ω cm^{-2}, 13.8 and 383.8 Ω cm^{-2}, 16.6 and 1530.0 Ω cm^{-2}, respectively. Here, the presence of RGO decreases the combined resistance of the working electrode and ionic resistance of the sacrificial reagent, increases the conductivity, hinders charge recombination, accelerates the charge transfer rate at the photoanode and electrolyte interface, thereby decreasing the both R_s and R_{ct} [70]. As a result, the lowest Rs and R_{ct} values of RGO(0.25)-$Cd_{0.8}Zn_{0.2}S_{0.2}Se_{0.8}$ can be attributed to high photoelectrochemical properties which is proven with the chronoamperometry experiments. The other EIS parameter values obtained from the data fitting are listed in Table S2.

Mott-Schottky (M-S) analysis is applied to clarify the band structure, identify the conductivity (n-type or p-type) and determine the flat band potential (V_{fb}) of a photoelectrode [71]. M-S analysis is performed at 100 Hz frequency in a dark condition [52]. According to Mott-Schottky (M-S) equation, (given in SM) [52], charge carrier density in the photoelectrode is inversely proportional to the slope of the linear portion of the M-S curve [72]. In Fig. 10, the slope of RGO(0.25)-$Cd_{0.8}Zn_{0.2}S_{0.2}Se_{0.8}$ is associated with its charge carrier density (charge donor density for n-type, N_D) and photocurrent. The positive slope of the photoelectrode suggests that it has an n-type conductivity [73]. The flat band potential value of RGO(0.25)-$Cd_{0.8}Zn_{0.2}S_{0.2}Se_{0.8}$ is obtained from the intercept of the linear part of the M-S plot. The flat band potential term provides a qualitative insight into the degree of band bending at the Schottky interface. The higher shift of band bending confirms that photoinduced charge recombination will be hard at the interface, and hence, photoelectrochemical performance can be significantly improved [74]. In this study, the highest shift of band bending belongs to the RGO (0.25)-$Cd_{0.8}Zn_{0.2}S_{0.2}Se_{0.8}$. Namely, the V_{fb} and N_D of RGO (0.25)-$Cd_{0.8}Zn_{0.2}S_{0.2}Se_{0.8}$ are estimated as −0.32 V vs. RHE and 4.44×10^{18} cm^{-3}, respectively. When compared with $Cd_{0.8}Zn_{0.2}S_{0.2}Se_{0.8}$ photoelectrode, the N_d value of RGO(0.25)-$Cd_{0.8}Zn_{0.2}S_{0.2}Se_{0.8}$ photoelectrode is 1.42 times higher, which is in accordance with our LSV, CA, and EIS results. There are no reports related to the N_D values of RGO—CdZnSSe photoelectrodes in the literature, yet a few reports are available for the N_D of CdZnSSe photoelectrodes. For instance, de Los Angeles Hernandez Perez et al. have calculated the N_D of $CdS_{0.25}Se_{0.75}$ as 1.39×10^{18} cm^{-3}, which is lower than our N_D value [8]. The determined V_{fb} and N_D values for $Cd_{0.8}Zn_{0.2}S$, $Cd_{0.8}Zn_{0.2}Se$, and $Cd_{0.8}Zn_{0.2}S_{0.2}Se_{0.8}$ photoelectrodes are given in Table S3.

Applied bias photon to current conversion efficiency (ABPE) value is directly related to the amount of energy utilized during reaction [75]. As shown in Fig. 11, the maximum ABPE values considering bias potential for $Cd_{0.8}Zn_{0.2}S_{0.2}Se_{0.8}$ and RGO(0.25)-$Cd_{0.8}Zn_{0.2}S_{0.2}Se_{0.8}$ are estimated as 2.15% and 3.07%, respectively.

Faradaic efficiencies for H_2 production are calculated based on Faraday's equation (SM). Experimental H_2 production rates for RGO(0.25)-$Cd_{0.8}Zn_{0.2}S_{0.2}Se_{0.8}$ and $Cd_{0.8}Zn_{0.2}S_{0.2}Se_{0.8}$ photoelectrodes are found as 85.2 and 59.1 μmol h^{-1}, respectively. By employing Faraday's equation for efficiency, FE% values are determined as 89.9% for RGO(0.25)-$Cd_{0.8}Zn_{0.2}S_{0.2}Se_{0.8}$ and 77.9% for $Cd_{0.8}Zn_{0.2}S_{0.2}Se_{0.8}$.

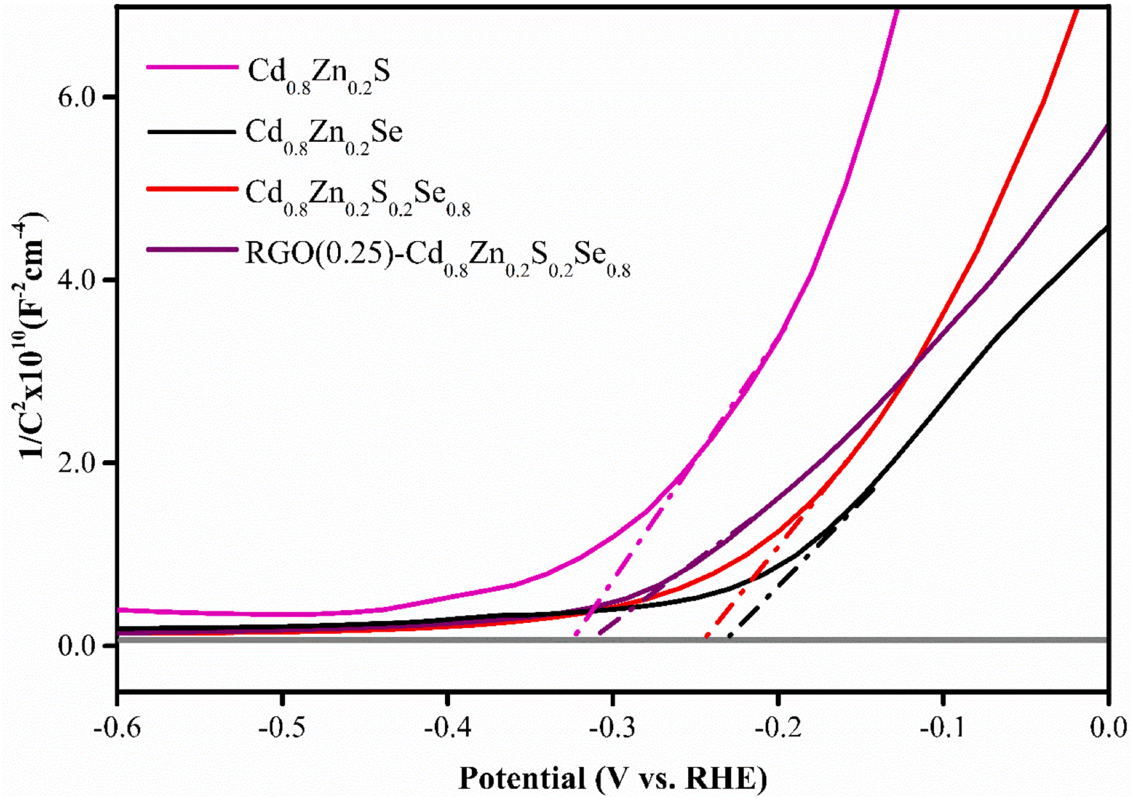

Fig. 10. M-S plots of $Cd_{0.8}Zn_{0.2}S$, $Cd_{0.8}Zn_{0.2}Se$, $Cd_{0.8}Zn_{0.2}S_{0.2}Se_{0.8}$, and RGO(0.25)-$Cd_{0.8}Zn_{0.2}S_{0.2}Se_{0.8}$ photoelectrodes.

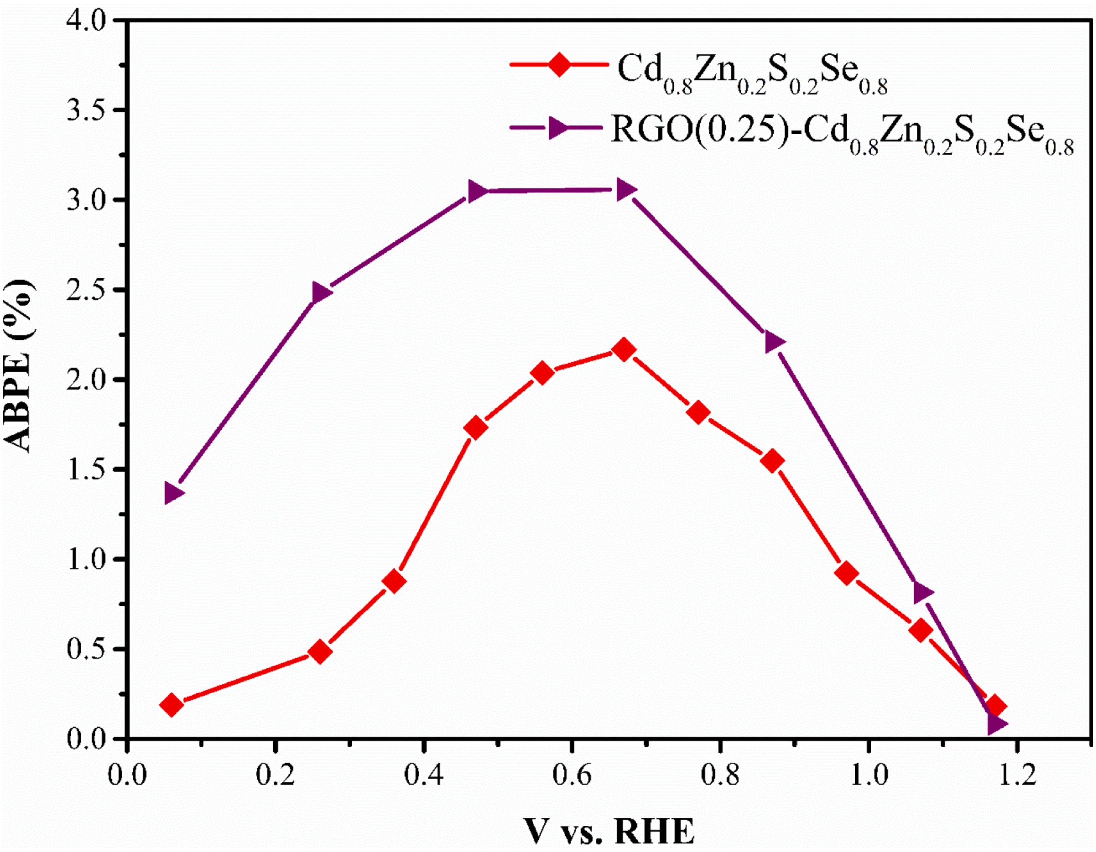

Fig. 11. ABPE values for $Cd_{0.8}Zn_{0.2}S_{0.2}Se_{0.8}$ and RGO(0.25)-$Cd_{0.8}Zn_{0.2}S_{0.2}Se_{0.8}$ photoelectrodes.

Fig. 12 displays a schematical representation of the band diagram of RGO(0.25)-$Cd_{0.8}Zn_{0.2}S_{0.2}Se_{0.8}$ photoelectrode and the mechanism of hydrogen production during PEC analysis in aqueous Na_2S/Na_2SO_3 sacrificial electrolyte. RGO(0.25)-$Cd_{0.8}Zn_{0.2}S_{0.2}Se_{0.8}$ behaves as a photoanode since it has excess electrons (e^-). When the photoanode is exposed to light, electrons are excited from the valence band (VB) to the conduction band (CB) followed by electron flow through the external circuit to the Pt cathode, leading to hydrogen production [76,77]. The positions of CB and VB are depicted as −0.46 eV and 1.35 eV vs. RHE, respectively. These values are obtained from M-S analysis and Tauc plot of Kubelka-Munk's function of RGO(0.25)-$Cd_{0.8}Zn_{0.2}S_{0.2}Se_{0.8}$ photoelectrode. During PEC hydrogen production in Na_2S/Na_2SO_3 sacrificial electrolyte, the oxidation and reduction reactions taking part are given as follows [78]:

Oxidation reactions:

$$SO_3^{2-} + 2OH^- + 2h^+ \rightarrow SO_4^{2-} + 2H^+ \tag{11}$$

$$2S^{2-} + 2h^+ \rightarrow S_2^{2-} \tag{12}$$

$$S_2^{2-} + SO_3^{2-} \rightarrow S_2O_3^{2-} + S^{2-} \tag{13}$$

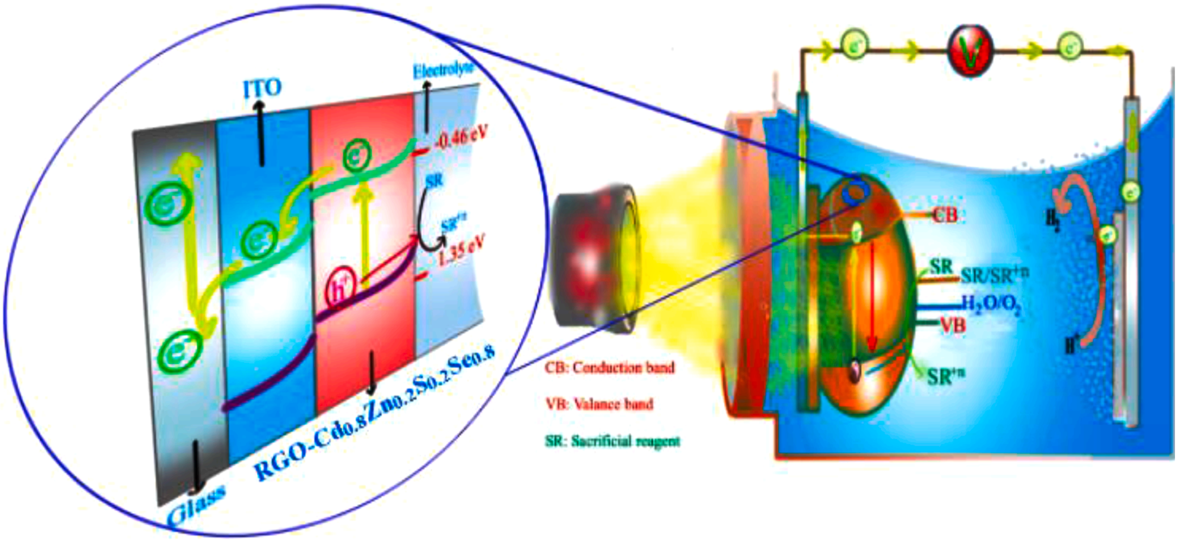

Fig. 12. Band diagram of RGO(0.25)-$Cd_{0.8}Zn_{0.2}S_{0.2}Se_{0.8}$ photoelectrode in PEC hydrogen production system.

$$SO_3^{2-} + S^{2-} + 2h^+ \rightarrow S_2O_3^{2-} \quad (14)$$

Reduction reaction at the Pt cathode:

$$2H^+ + 2e^- \rightarrow H_2 \quad (15)$$

Mehtab et al. studied the photocatalytic and the photoelectrochemical water splitting process in the presence of an alkaline Na_2S/Na_2SO_3 sacrificial reagent and reported the potential of the overall Na_2S/Na_2SO_3 oxidation reaction as 0.936 eV. This potential falls across −0.46 eV-1.35 eV, which correspond to the conduction band and valence band values, respectively, making the oxidation reactions possible within this potential range [79].

At the valence band of the photoelectrode, SO_3^{2-} and S^{2-} ions of sacrificial electrolyte react with holes to give H^+ and S_2^{2-} ions in the basic medium. Excess SO_3^{2-} and S^{2-} ions originated from the sacrificial electrolyte and produced S_2^{2-} form $S_2O_3^{2-}$ simultaneously. H_2 gas is generated at the cathode side (Pt wire) of the three-electrode system.

4. Conclusions

This study systematically investigates the facile one-step electrodeposition and photoelectrochemical activity of $Cd_{0.8}Zn_{0.2}S_xSe_{1-x}$ and RGO—$Cd_{0.8}Zn_{0.2}S_{0.2}Se_{0.8}$ for the first time in literature. With this new method, RGO—$Cd_{0.8}Zn_{0.2}S_{0.2}Se_{0.8}$ composite structure can be easily coated on the electrode surface at room temperature with easy control. Immobilization of $Cd_{0.8}Zn_{0.2}S_{0.2}Se_{0.8}$ particles among RGO sheets enhances immobilization strength, film conductivity, and consequently photoelectrochemical performance of it as an n-type photoelectrode. The results of photoelectrochemical analyses reveal that $Cd_{0.8}Zn_{0.2}S_{0.2}Se_{0.8}$ photoelectrode exhibits the highest photocurrent density of 4.08 mA cm^{-2} among $Cd_{0.8}Zn_{0.2}S_xSe_{1-x}$ ($x = 0$, 0.2, 0.5, 0.8, 1.0) photoelectrodes. In addition, including RGO in the $Cd_{0.8}Zn_{0.2}S_{0.2}Se_{0.8}$ structure suppresses the recombination of photoinduced charges and consequently enhances the photoelectrochemical activity. Yet, high amounts of RGO may block the light absorption of the photoelectrode and cut down the yield of photocurrent density. A 9.8% decrease in the photocurrent density of RGO(0.25)-$Cd_{0.8}Zn_{0.2}S_{0.2}Se_{0.8}$ is reported when RGO(0.50)-$Cd_{0.8}Zn_{0.2}S_{0.2}Se_{0.8}$ is tested in chronoamperometric analyses, which may result from decreasing of the concentration of sacrificial reagent during PEC reaction. Finally, the photocurrent density and ABPE of RGO(0.25)-$Cd_{0.8}Zn_{0.2}S_{0.2}Se_{0.8}$ photoelectrode are estimated as 5.00 mA cm^{-2} and 3.07%, respectively. Characterization results of the photoelectrodes with respect to XPS, diffuse reflectance, and EIS responses endorse the best performance of RGO(0.25)-$Cd_{0.8}Zn_{0.2}S_{0.2}Se_{0.8}$ composite. The high photoelectrochemical performance results of $Cd_{0.8}Zn_{0.2}S_{0.2}Se_{0.8}$ and RGO (0.25)-$Cd_{0.8}Zn_{0.2}S_{0.2}Se_{0.8}$ can also associate with the R_s values obtained from EIS measurements which are lower than the other investigated photoelectrodes. Furthermore, these results can be supported with the higher N_D values of $Cd_{0.8}Zn_{0.2}S_{0.2}Se_{0.8}$ and RGO(0.25)-$Cd_{0.8}Zn_{0.2}S_{0.2}Se_{0.8}$ determined from the M-S tests. RGO—CdZnSSe based photoelectrodes fabricated by a facile one-step electrodeposition technique can ultimately improve the photoelectrochemical activity, providing a progressive framework for hydrogen production.

CRediT authorship contribution statement

Özlem UĞUZ NELİ: Conceptualization, Methodology, Validation, Writing – original draft. **Özlem BUDAK:** Conceptualization, Methodology, Validation, Writing – original draft. **Atıf KOCA:** Conceptualization, Investigation, Resources, Supervision, Funding acquisition, Writing – review & editing.

Declaration of Competing Interest

The authors declare that they have no known competing financial interests or personal relationships that could have appeared to influence the work reported in this paper.

Data availability

No data was used for the research described in the article.

Acknowledgments

This work is supported by The Scientific and Technological Research Council of Turkey (TUBITAK) [Grant Number: 219M328] and Scientific Research Projects Commission (BAPKO) of Marmara University [Grant Number: FDK-2020–10022]. Atıf Koca also thanks to the Turkish Academy of Sciences (TÜBA) for the financial support.

Supplementary materials

Supplementary material associated with this article can be found, in the online version, at doi:10.1016/j.electacta.2023.142495.

References

[1] Ö. Uğuz, Ö. Budak, A. Koca, Simultaneous electrodeposition of electrochemically reduced graphene oxide-binary metal chalcogenide composites to enhance photoelectrochemical performance, Int. J. Hydrogen. Energy (2021), https://doi.org/10.1016/j.ijhydene.2021.08.064.

[2] P. Wang, S. Wang, L. Gao, X. Long, H. Chai, F. Li, Q. Wang, J. Jin, Achieving surface-sealing of hematite nanoarray photoanode with controllable metal–organic frameworks shell for enhanced photoelectrochemical water oxidation, J. Catal 413 (2022) 398–406, https://doi.org/10.1016/j.jcat.2022.06.04.

[3] T. Tian, C. Dong, X. Liang, M. Yue, Y. Ding, Enhanced photoelectrochemical water oxidation activity of BiVO4 by coating of Co-phenolic networks as hole-transfer and co-catalyst, J. Catal 377 (2019) 684–691, https://doi.org/10.1016/j.jcat.2019.08.012.

[4] V. Sharma, A.C. Dakshinamurthy, B. Pandey, S.C. Roy, C. Sudakar, Highly efficient photoelectrochemical ZnO and TiO2 nanorod/Sb2S3 heterostructured photoanodes through one step thermolysis of Sb-MPA complex, Solar Energy 225 (2021) 333–343, https://doi.org/10.1016/j.solener.2021.07.045.

[5] A.A.A. Abdelazeez, A.B.G. Trabelsi, F.H. Alkallas, M. Rabia, Successful 2D MoS2 nanosheets synthesis with SnSe grid-like nanoparticles: photoelectrochemical hydrogen generation and solar cell applications, Solar Energy 248 (2022) 251–259, https://doi.org/10.1016/j.solener.2022.10.058.

[6] Y. Chen, X. Ren, K. Zhang, L. Wang, Structure and photoluminescence of ZnS/CdS1-xSex nanocomposite prepared by a two-step process, Mater. Sci. Semicond. Process 100 (2019) 42–47.

[7] P. Ravi, V.N. Rao, M. Shankar, M. Sathish, Heterojunction engineering at ternary Cu2S/Ta2O5/CdS nanocomposite for enhanced visible light-driven photocatalytic hydrogen evolution, Mater. Today Energy 21 (2021), 100779, https://doi.org/10.1016/j.mtener.2021.100779.

[8] de los Angeles Hernandez-Perez, M., Sanchez-Ramirez, E.A., Castillo-Plata, F.J., Manzo-Robledo, A., Aguilar-Hernandez, J.R., Ezeta-Mejia, A., Sastre-Hernandez, J., Ramirez-Meneses, E., Villanueva-Ibañez, M., and Flores-Caballero, A.A., Photoelectrochemical properties of chemically deposited cadmium sulphoselenide (CdS1-xSex/ITO) thin films. Vacuum, 2020. 175: p. 109277. https://doi.org/10.1016/j.vacuum.2020.109277.

[9] R. Chong, Z. Wang, J. Lv, J. Rong, L. Zhang, Y. Jia, L. Wang, Z. Chang, X. Wang, A hybrid CoOOH-rGO/Fe2O3 photoanode with spatial charge separation and charge transfer for efficient photoelectrochemical water oxidation, J. Catal 399 (2021) 170–181, https://doi.org/10.1016/j.jcat.2021.05.006.

[10] L. Li, B. Li, H. Liu, M. Li, B. Wang, Photoelectrochemical sensing of hydrogen peroxide using TiO2 nanotube arrays decorated with RGO/CdS, J. Alloys. Compd 815 (2020), 152241, https://doi.org/10.1016/j.jallcom.2019.152241.

[11] H. Li, C. Sun, Y. Zhao, X. Xu, H. Yu, Facile synthesis of recyclable Co 3 O 4/Co (OH) 2/RGO ternary heterostructures with synergistic effect for photocatalysis, J. Nanopar. Res. 20 (10) (2018) 1–13, https://doi.org/10.1007/s11051-018-4359-3.

[12] V.S. Raut, C.D. Lokhande, V.V. Killedar, Synthesis and studies on effect of indium doping on physical properties of electrodeposited CdSe thin films, J. Mater. Sci 28 (4) (2017) 3140–3150, https://doi.org/10.1007/s10854-016-5902-6.

[13] A. Ojo, I. Dharmadasa, Analysis of electrodeposited CdTe thin films grown using cadmium chloride precursor for applications in solar cells, J. Mater. Sci. 28 (19) (2017) 14110–14120, https://doi.org/10.1007/s10854-017-7264-0.

[14] Sharma, V., Prasad, M., Ilaiyaraja, P., Sudakar, C., and Jadkar, S., Electrodeposition of highly porous ZnO nanostructures with hydrothermal amination for efficient photoelectrochemical activity. Int. J. Hydrogen Energy, 2019. 44(23): p. 11459–11471. https://doi.org/10.1016/j.ijhydene.2019.03.132.

[15] S. Ibrahim, K. Chakraborty, T. Pal, S. Ghosh, Reduced graphene oxide–cadmium zinc sulfide nanocomposite with controlled band gap for large-area thin-film

optoelectronic device application, J. Mater. Eng. Perform 27 (2018) 2629–2634, https://doi.org/10.1007/s11665-017-3082-z.

[16] H. Zhuang, X. Liu, F. Li, W. Xu, L. Lin, Z. Cai, Construction of CdSe@ TiO2 core-shell nanorod arrays by electrochemical deposition for efficient visible light photoelectrochemical performance, Int. J. Energy. Res. 43 (13) (2019) 7197–7205, https://doi.org/10.1002/er.4744.

[17] A.K. Ayal, Z. Zainal, H.N. Lim, Z.A. Talib, Y.-.C. Lim, S.-.K. Chang, A.M. Holi, Fabrication of CdSe nanoparticles sensitized TiO2 nanotube arrays via pulse electrodeposition for photoelectrochemical application, Mater. Res. Bull 106 (2018) 257–262, https://doi.org/10.1016/j.materresbull.2018.05.040.

[18] M. Izi, G. Heidari, S.M. Khoie, J. Najafi, Comparison of ZnS thin films fabricated by electrodeposition and spray pyrolysis methods, Surface Engin. Appl. Electrochem. 53 (3) (2017) 245–249, https://doi.org/10.3103/S1068375517030085.

[19] W. Kumarage, R. Wijesundera, N. Kaur, D. Zappa, V. Seneviratne, C. Jayalath, B. Dassanayake, A Comparative Assessment: chemical Bath Deposited and Electrodeposited CdS Films, Int. J. Electro. Mater 7 (2019) 1–6.

[20] G. Riveros, C. Baez, D. Ramírez, C.J. Pereyra, R.E. Marotti, R. Romero, F. Martín, J. R. Ramos-Barrado, E.A. Dalchiele, Electrodeposition and characterization of composition-graded CdSxSe (1–x) multilayer thin film structures, J. Alloys. Compd 686 (2016) 235–244, https://doi.org/10.1016/j.jallcom.2016.06.010.

[21] M. Cao, K. Yao, Z. Chen, Y. Guan, X. Zhang, J. Huang, Y. Sun, J. Lai, M. Chen, L. Wang, Enhanced photoelectrochemical water splitting with template-free electrodeposition of SnS nanorods photoelectrode, J. Alloys. Compd 830 (2020), 154729, https://doi.org/10.1016/j.jallcom.2020.154729.

[22] K. Matoba, Y. Matsuda, M. Takahashi, Y. Sakata, J. Zhang, S. Higashimoto, Fabrication of Pt/In2S3/CuInS2 thin film as stable photoelectrode for water splitting under solar light irradiation, Catal. Today 375 (2021) 87–93, https://doi.org/10.1016/j.cattod.2020.01.015.

[23] F.E. Osterloh, Inorganic materials as catalysts for photochemical splitting of water, Chem. Mater. 20 (1) (2008) 35–54, https://doi.org/10.1021/cm7024203.

[24] A. Kudo, Y. Miseki, Heterogeneous photocatalyst materials for water splitting, Chem. Soc. Rev 38 (1) (2009) 253–278, https://doi.org/10.1039/B800489G.

[25] J. Kim, T. Minegishi, J. Kobota, K. Domen, Enhanced photoelectrochemical properties of CuGa 3 Se 5 thin films for water splitting by the hydrogen mediated co-evaporation method, Energy Environ. Sci 5 (4) (2012) 6368–6374, https://doi.org/10.1039/C1EE02280F.

[26] C. Camus, N. Allsop, S. Gledhill, W. Bohne, J. Röhrich, I. Lauermann, M. Lux-Steiner, C.-.H. Fischer, Properties of spray ILGAR CuInS2 thin films, Thin Solid Films 516 (20) (2008) 7026–7030, https://doi.org/10.1016/j.tsf.2007.12.069.

[27] J. Zhao, T. Minegishi, L. Zhang, M. Zhong, M. Nakabayashi, G. Ma, T. Hisatomi, M. Katayama, S. Ikeda, N. Shibata, Enhancement of solar hydrogen evolution from water by surface modification with CdS and TiO2 on porous CuInS2 photocathodes prepared by an electrodeposition–sulfurization method, Angewandte. Chemie. Int. Edition 53 (44) (2014) 11808–11812, https://doi.org/10.1002/anie.201406483.

[28] R.Z. Ayaz, D. Akyüz, Ö. Uğuz, İ. Tanşık, C. Sarıoğlu, F. Karaca, A.R. Özkaya, A. Koca, Photoelectrochemical performance of thermally sulfurized CdxZn1-xS photoanode: enhancement with reduced graphene oxide support, Renew. Energy 162 (2020) 182–195, https://doi.org/10.1016/j.renene.2020.07.102.

[29] Ö. Uğuz, Ö. Budak, A. Koca, Simultaneous electrodeposition of electrochemically reduced graphene oxide-binary metal chalcogenide composites to enhance photoelectrochemical performance, Int. J. Hydrogen. Energy 46 (71) (2021) 35290–35301, https://doi.org/10.1016/j.ijhydene.2021.08.064.

[30] D.C. Marcano, D.V. Kosynkin, J.M. Berlin, A. Sinitskii, Z. Sun, A. Slesarev, L. B. Alemany, W. Lu, J.M. Tour, Improved synthesis of graphene oxide, ACS. Nano 4 (8) (2010) 4806–4814, https://doi.org/10.1021/nn1006368.

[31] G.R. Bhand, N.B. Chaure, Synthesis of CdTe, CdSe and CdTe/CdSe core/shell QDs from wet chemical colloidal method, Mater. Sci. Semicond. Process 68 (2017) 279–287, https://doi.org/10.1016/j.mssp.2017.06.033.

[32] N. Hidayah, W.-.W. Liu, C.-.W. Lai, N. Noriman, C.-.S. Khe, U. Hashim, H.C. Lee, Comparison on graphite, graphene oxide and reduced graphene oxide: synthesis and characterization, in: AIP Conference Proceedings, AIP Publishing LLC, 2017, https://doi.org/10.1063/1.5005764.

[33] S. Monika, M. Mahalakshmi, K. Veerathangam, M. Senthil Pandian, P. Ramasamy, Conductive carbon black/CuS composite counter electrode for the enhanced photovoltaic performance of CdS quantum dot sensitized solar cells, Appl. Phys. A 128 (3) (2022) 1–13, https://doi.org/10.1007/s00339-022-05356-9.

[34] Z. Wei, W. Mao, J. Liu, Y. Xiao, M. Zhu, Y. Tian, CdS nanorods decorated with ultrathin MoS 2 nanosheets for efficient visible-light photocatalytic H 2 production, J. Mater. Sci. 31 (6) (2020) 4574–4581, https://doi.org/10.1007/s10854-020-03008-3.

[35] Q.-.S. Jiang, W. Li, J. Wu, W. Cheng, J. Zhu, Z. Yan, X. Wang, Y. Ju, Electrodeposited cobalt and nickel selenides as high-performance electrocatalytic materials for dye-sensitized solar cells, J. Mater. Sci. 30 (10) (2019) 9429–9437, https://doi.org/10.1007/s10854-019-01273-5.

[36] H. Nie, L. Fu, J. Zhu, W. Yang, D. Li, L. Zhou, Excellent tribological properties of lower reduced graphene oxide content copper composite by using a one-step reduction molecular-level mixing process, Materials. (Basel) 11 (4) (2018) 600, https://doi.org/10.3390/ma11040600.

[37] V.R. Moreira, Y.A.R. Lebron, M.M. da Silva, L.V. de Souza Santos, R.S. Jacob, C.K. B. de Vasconcelos, M.M. Viana, Graphene oxide in the remediation of norfloxacin from aqueous matrix: simultaneous adsorption and degradation process, Environmen. Sci. Pollu. Res. 27 (27) (2020) 34513–34528, https://doi.org/10.1007/s11356-020-09656-6.

[38] M. Sharma, S. Sen, J. Gupta, M. Ghosh, S. Pitale, V. Gupta, S. Gadkari, Tunable blue-green emission from ZnS (Ag) nanostructures grown by hydrothermal synthesis, J. Mater. Res 33 (23) (2018) 3963–3970, https://doi.org/10.1557/jmr.2018.358.

[39] Y. Lei, Y. He, C. Fang, Composition-tunable ternary CdS1− xSex/graphene composites with enhanced photocurrent response, J. Mater. Sci. 28 (1) (2017) 878–883, https://doi.org/10.1007/s10854-016-5602-2.

[40] H. Dhaygude, S.K. Shinde, D. Dubal, N.B. Velhal, D.-.Y. Kim, V. Fulari, Structural, optical, and photoelectrochemical properties of nanosphere-like CdXZn1-XS synthesized by electrochemical route, Ionics. (Kiel) 23 (1) (2017) 223–231, https://doi.org/10.1007/s11581-016-1797-8.

[41] N.P. Anh, H.T.K. Chi, N. Tri, H.T.K. Dung, Photoactivity of reducing graphene oxide and titanium dioxide composite for cinnamic acid degradation, Mater. Transac. 59 (7) (2018) 1117–1123, https://doi.org/10.2320/matertrans.MD201721.

[42] A. Shanmugasundaram, M.A. Johar, R. Boppella, D.-.S. Kim, Y.-.J. Jeong, J.Y. Kim, M.A. Hassan, S.-.W. Ryu, D.W. Lee, Stabilizing nanocrystalline Cu2O with ZnO/rGO: engineered photoelectrodes enables efficient water splitting, Ceram. Int 47 (6) (2021) 7558–7570, https://doi.org/10.1016/j.ceramint.2020.11.094.

[43] B. Zhang, X. Ma, J. Ma, Y. Zhou, G. Liu, D. Ma, Z. Deng, M. Luo, Y. Xin, Fabrication of rGO and g-C3N4 co-modified TiO2 nanotube arrays photoelectrodes with enhanced photocatalytic performance, J. Colloid. Interface. Sci 577 (2020) 75–85, https://doi.org/10.1016/j.jcis.2020.05.031.

[44] S. Zhao, J. Xu, H. Yu, Z. Liu, Y. Li, RGO boosts band gap regulates for constructing Ni2P/RGO/MoO2 Z-scheme heterojunction to achieve high efficiency photocatalytic H2 evolution, Catal. Lett. 149 (11) (2019) 3012–3026, https://doi.org/10.1007/s10562-019-02872-x.

[45] C. Ng, J.-.H. Yun, H.L. Tan, H. Wu, R. Amal, Y.H. Ng, A dual-electrolyte system for photoelectrochemical hydrogen generation using CuInS 2-In 2 O 3-TiO 2 nanotube array thin film, Science. China. Materials 61 (6) (2018) 895–904, https://doi.org/10.1007/s40843-017-9237-2.

[46] D. Yan, X. Fu, Z. Shang, J. Liu, H.a. Luo, A BiVO4 film photoanode with re-annealing treatment and 2D thin Ti3C2TX flakes decoration for enhanced photoelectrochemical water oxidation, Chem. Engin. J. 361 (2019) 853–861, https://doi.org/10.1016/j.cej.2018.12.146.

[47] Y. Hou, Z. Ahmed Syed, L. Jiu, J. Bai, T. Wang, Porosity-enhanced solar powered hydrogen generation in GaN photoelectrodes, Appl. Phys. Lett 111 (20) (2017), 203901, https://doi.org/10.1063/1.5001938.

[48] C. Jia, X. Gu, Y. Zhao, L. Wang, Y. Qiang, Enhanced photoelectrochemical performance of black Si electrode by forming a pn junction, J. Mater.. Sci. 29 (24) (2018) 20734–20741, https://doi.org/10.1007/s10854-018-0214-7.

[49] X. Zhang, X. Bian, H. Xu, W. Wu, Fabrication of WO3/RGO/Ni: feOOH heterostructure for synergistically enhancing photoelectrochemical water oxidation, Appl. Surf. Sci 542 (2021), 148579, https://doi.org/10.1016/j.apsusc.2020.148579.

[50] Q. Shi, X. Song, H. Wang, Z. Bian, Enriched photoelectrochemical performance of phosphate doped BiVO4 photoelectrode by coupling FeOOH and rGO, J. Electrochem. Soc 165 (4) (2017) H3018, https://doi.org/10.1149/2.0021804jes.

[51] M. Nasiri, P. Sangpour, S. Yousefzadeh, M. Bagheri, Elevated temperature annealed α-Fe2O3/reduced graphene oxide nanocomposite photoanode for photoelectrochemical water oxidation, J. Environ. Chem. Eng 7 (2) (2019), 102999, https://doi.org/10.1016/j.jece.2019.102999.

[52] R. Ranjan, M. Kumar, A. Sinha, Development and characterization of rGO supported CdSMoS2 photoelectrochemical catalyst for splitting water by visible light, Int. J. Hydrogen. Energy 44 (31) (2019) 16176–16189, https://doi.org/10.1016/j.ijhydene.2019.03.126.

[53] Vishwakarma, M., Batra, Y., Hadermann, J., Singh, A., Ghosh, A., and Mehta, B., Exploring the Role of Graphene Oxide as a Co-Catalyst in the CZTS Photocathodes for Improved Photoelectrochemical Properties. ACS. Appl. Energy Mater.,. 2022. https://doi.org/10.1021/acsaem.2c01011.

[54] C.S. Yaw, W.C. Ng, Q. Ruan, J. Tang, A.K. Soh, M.N. Chong, Tuning of reduced graphene oxide thin film as an efficient electron conductive interlayer in a proven heterojunction photoanode for solar-driven photoelectrochemical water splitting, J. Alloys. Compd 817 (2020), 152721, https://doi.org/10.1016/j.jallcom.2019.152721.

[55] Y.-.H. Zhang, X.-.L. Cai, D.-.Y. Guo, H.-.J. Zhang, N. Zhou, S.-.M. Fang, J.-.L. Chen, H.-.L. Zhang, Oxygen vacancies in concave cubes Cu 2 O-reduced graphene oxide heterojunction with enhanced photocatalytic H 2 production, J. Mater. Sci. 30 (7) (2019) 7182–7193, https://doi.org/10.1007/s10854-019-01036-2.

[56] G. Liu, Z. Ling, Y. Wang, H. Zhao, Near-infrared CdSexTe1-x@ CdS "giant" quantum dots for efficient photoelectrochemical hydrogen generation, Int. J. Hydrogen. Energy 43 (49) (2018) 22064–22074, https://doi.org/10.1016/j.ijhydene.2018.10.076.

[57] M.N. Shaddad, D. Cardenas-Morcoso, P. Arunachalam, M. García-Tecedor, M. A. Ghanem, J. Bisquert, A. Al-Mayouf, S. Gimenez, Enhancing the optical absorption and interfacial properties of BiVO4 with Ag3PO4 nanoparticles for efficient water splitting, J. Phys. Chem. C 122 (22) (2018) 11608–11615, https://doi.org/10.1021/acs.jpcc.8b00738.

[58] F. Navarro-Pardo, H. Zhao, Z.M. Wang, F. Rosei, Structure/property relations in "giant" semiconductor nanocrystals: opportunities in photonics and electronics, Acc.. Chem.. Res. 51 (3) (2017) 609–618, https://doi.org/10.1021/acs.accounts.7b00467.

[59] C. Li, Y. Wang, S. Chen, W. Zhang, Z. Wang, Z. Hou, Enhanced photoelectrochemical performance based on conformal and uniform ZnO/ZnSe/CdSe heterostructures on Zn foil substrate, Int. J. Hydrogen. Energy 45 (15) (2020) 8257–8272, https://doi.org/10.1016/j.ijhydene.2020.01.069.

[60] J. Han, S. Zhang, Q. Song, H. Yan, J. Kang, Y. Guo, Z. Liu, The synergistic effect with S-vacancies and built-in electric field on a TiO 2/MoS 2 photoanode for enhanced photoelectrochemical performance, Sustain. Energy Fuels 5 (2) (2021) 509–517, https://doi.org/10.1039/D0SE01515F.

[61] W. Zhang, Q. Zhong, X. Liu, Q. Lu, Inorganic functionalization of CdSexS1−x/ZnS core–shell quantum dots and their photoelectric properties, Physica. Status. solidi. (a) 217 (11) (2020), 2000010, https://doi.org/10.1002/pssa.202000010.

[62] M. Lin, W. Wang, Passivation of ZnSe nanoparticles in sandwiched CdSe/ZnSe/ZnO nanotube array photoanode to substantially enhance solar photoelectrochemical water splitting for hydrogen evolution, Colloids Surfaces. A 614 (2021), 126206, https://doi.org/10.1016/j.colsurfa.2021.126206.

[63] Z. Ye, Z. Hu, L. Yang, X. Xiao, Stable p-type Cu: cdS1− xSex/Pt Thin-Film Photocathodes with Fully Tunable Bandgap for Scavenger-Free Photoelectrochemical Water Splitting, Solar. RRL 4 (3) (2020), 1900567, https://doi.org/10.1002/solr.201900567.

[64] Z. Masoumi, M. Tayebi, B.-.K. Lee, Ultrasonication-assisted liquid-phase exfoliation enhances photoelectrochemical performance in α-Fe2O3/MoS2 photoanode, Ultrason. Sonochem 72 (2021), 105403, https://doi.org/10.1016/j.ultsonch.2020.105403.

[65] S. Saxena, A. Verma, K. Asha, N.K. Biswas, A. Srivastav, V.R. Satsangi, R. Shrivastav, S. Dass, BiVO 4/Fe 2 O 3/ZnFe 2 O 4; triple heterojunction for an enhanced PEC performance for hydrogen generation, RSC. Adv., 12 (20) (2022) 12552–12563, https://doi.org/10.1039/D2RA00900E.

[66] Z. Cao, Y. Yin, P. Fu, D. Li, Y. Zhou, Y. Deng, Y. Peng, W. Wang, W. Zhou, D. Tang, TiO 2 nanosheet arrays with layered SnS 2 and CoO x nanoparticles for efficient photoelectrochemical water splitting, Nanoscale. Res. Lett 14 (1) (2019) 1–9, https://doi.org/10.1186/s11671-019-3168-7.

[67] S.S. Bhat, S.A. Pawar, D. Potphode, C.-.K. Moon, J.M. Suh, C. Kim, S. Choi, D. S. Patil, J.-.J. Kim, J.C. Shin, Substantially enhanced photoelectrochemical performance of TiO2 nanorods/CdS nanocrystals heterojunction photoanode decorated with MoS2 nanosheets, Environmental 259 (2019), 118102, https://doi.org/10.1016/j.apcatb.2019.118102.

[68] I.N. Reddy, C.V. Reddy, K. Ravindranadh, M. Cho, D. Kim, J. Shim, A study of coral reef-like tetragonal Mn3O4 nanostructure photoelectrode for photoelectrochemical water splitting under visible irradiation, J. Electroanal. Chem. 874 (2020), 114488, https://doi.org/10.1016/j.jelechem.2020.114488.

[69] X. Li, Y. Li, H. Wang, H. Miao, H. Zhu, X. Liu, H. Lin, G. Shi, Fabrication of a three-dimensional bionic Si/TiO2/MoS2 photoelectrode for efficient solar water splitting, ACS. Appl. Energy. Mater. 4 (1) (2020) 730–736, https://doi.org/10.1021/acsaem.0c02594.

[70] J. Xu, W. Sun, Z. Hu, Y. You, Y. Lu, R. Zhou, J. Zhang, Green and room-temperature synthesis of aqueous CuInS2 and Cu2SnS3 nanocrystals for efficient photoelectrochemical water splitting, Mater. Today Energy 10 (2018) 200–207, https://doi.org/10.1016/j.mtener.2018.09.010.

[71] K. Atacan, N. Güy, B. Boutra, M. Özacar, Enhancement of photoelectrochemical hydrogen production by using a novel ternary Ag2CrO4/GO/MnFe2O4 photocatalyst, Int. J. Hydrogen. Energy 45 (35) (2020) 17453–17467, https://doi.org/10.1016/j.ijhydene.2020.04.268.

[72] L. Meng, S. Wang, F. Cao, W. Tian, R. Long, L. Li, Doping-induced amorphization, vacancy, and gradient energy band in SnS2 nanosheet arrays for improved photoelectrochemical water splitting, Angewandte. Chemie 131 (20) (2019) 6833–6837, https://doi.org/10.1002/ange.201902411.

[73] X. Luo, Y. Xiao, B. Zhang, C. Feng, Z. Fan, Y. Li, Direct synthesis of BaTaO2N nanoparticle film on a conductive substrate for photoelectrochemical water splitting, J. Catal (2022), https://doi.org/10.1016/j.jcat.2022.05.005.

[74] S. Kumar, S. Ahirwar, A.K. Satpati, Insight into the PEC and interfacial charge transfer kinetics at the Mo doped BiVO 4 photoanodes, RSC. advances, 9 (70) (2019) 41368–41382, https://doi.org/10.1039/C9RA08743E.

[75] S. Gopalakrishnan, K. Jeganathan, Facile fabrication of silicon nanowires as photocathode for visible-light induced photoelectrochemical water splitting, Int. J. Hydrogen. Energy 42 (36) (2017) 22671–22676, https://doi.org/10.1016/j.ijhydene.2017.07.148.

[76] M. Ahmed, I. Dincer, A review on photoelectrochemical hydrogen production systems: challenges and future directions, Int. J. Hydrogen. Energy 44 (5) (2019) 2474–2507, https://doi.org/10.1016/j.ijhydene.2018.12.037.

[77] A. Kathalingam, S. Valanarasu, S. Ramesh, H.S. Kim, H.-.S. Kim, Photoelectrochemical solar cell study of electrochemically synthesized Cd1-xZnxTe thin films, Solar. Energy 224 (2021) 923–929, https://doi.org/10.1016/j.solener.2021.06.065.

[78] M. Wang, S. Shen, L. Li, Z. Tang, J. Yang, Effects of sacrificial reagents on photocatalytic hydrogen evolution over different photocatalysts, J. Mater. Sci 52 (2017) 5155–5164, https://doi.org/10.1007/s10853-017-0752-z.

[79] A. Mehtab, S.M. Alshehri, T. Ahmad, Photocatalytic and photoelectrocatalytic water splitting by porous g-C3N4 nanosheets for hydrogen generation, ACS. Appl. Nano. Mater. 5 (9) (2022) 12656–12665, https://doi.org/10.1021/acsanm.2c02460.